Two-dimensional Separated Flow Model around Ship Cross-sections

by

UENO Michio*

Abstract

This study is on an application of Parkinson's wake source model for analyzing the potential flow around ship cross-sections. The Lewis form is used to approximate the ship cross-sections. The analysis presented here demonstrates the difficulties of applying the wake source model, which mainly occur in flow which separates around the upstream bilge corner of thick cross-sections or the center keel of thin cross-sections. The present study aims also to enhance the wake source model and overcome these difficulties. Applications of the extended wake source model to cross-sections of a containership and a tanker show appropriate separation streamlines and pressure distributions of cross-sections with adequate Lewis form approximations. In addition, this study discusses the effects of the separation point and the base pressure in the downstream region on the drag coefficient of ship cross-sections. The sectional drag coefficient distributions along the ship's length are compared with the tank test data of segmented ship models to validate the extended wake source model.

＊　Senior director for research

原稿受付　令和 5年 6月　2日
審 査 日　令和 5年 9月　7日

Contents

1. Introduction

The shortage of seafarers and the need for higher navigation safety have been promoting the development of autonomous ships. The technologies together with rules and regulations are going to be in a phase of the practical use of autonomous ships. The most difficult situations for autonomous ships are berthing and unberthing. The lateral speed and yaw rate of ships compared with the longitudinal speed can be quite larger in these situations than those in ocean-going conditions. Wind and currents effects on ship motion tend to be larger in these situations because of slow ship speed. Therefore, they must pay special attention to the control of autonomous ships in such situations.

The cross-flow model[1,2] is one of the mathematical models that represent hydrodynamic forces acting on ships in manoeuvring motion. The hydrodynamic force in the cross-flow model is based on two-dimensional flow across ship sections normal to the centerline. This is the reason why the cross-flow model is suitable for describing low-speed manoeuvres and for controlling autonomous ships in berthing and unberthing situations[3,4].

Many researchers have used the cross-flow model in the equations of motion of ships[3-7]. However, theoretical studies analyzing two-dimensional flow around ship cross-sections and estimating cross-flow drags are not many. The cross-flow drag coefficient plays an important role in the equations and resultant ship motion. Kijima and Tanaka[8,9] used the vortex shedding model to analyze the two-dimensional flow around rectangular sections with and without round corners and estimated cross-flow drag coefficients. Tanaka and Kijima[10] applied their method to ship cross-sections and compared them with tank test data of a segmented ship model[11,12].

This paper presents a study on an application of Parkinson's wake source model[13] to potential flow around ship cross-sections. Lewis form[14] approximates the ship cross-sections. The analysis presented here clarifies that the wake source model has difficulties in the application. The difficulties mainly occur in such flow as separates around upstream bilge corner of thick cross-sections or center keel of thin cross-sections. The present study enhances the wake source model and resolves the difficulties. Applications of the enhanced wake source model to a containership and a tanker show appropriate separation streamlines and pressure distributions of cross-sections with adequate Lewis form approximations. The study discusses the effect of the separation point and the base pressure in the downstream region on the drag coefficient of the ship cross-sections. Comparisons of the sectional drag coefficient distributions along ship length with tank test data of the segmented ship models[11,12] validate the extended wake source model.

Note that this paper presents part of the study carried out when the author was in the graduate school of Osaka University in a more detailed manner than Ueno[15] with additional consideration.

2. Formulation

Parkinson and Jandali[13] presented the wake source model to represent two-dimensional separated flow around bluff bodies. They considered the incompressible and irrotational steady flow. The bluff bodies were a normal flat plate, a circular cylinder, a 90-degree wedge, and an elliptical cylinder placed symmetrically to the incident flow. In this paper, the Lewis form transformation[14] transforms the separated flow around circular cylinders into those around ship cross-sections.

2.1 Separated flow around a circular cylinder

2.1.1 Basic transform plane of the wake source model

The basic transform plane, ζ-pl., is a complex plane shown in Fig. 2.1.1 Variables $(r,\ \theta)$ and $(\xi,\ \eta)$ represent polar and orthogonal coordinates of an arbitrary point, respectively. The flow in the ζ-pl. consists of a uniform flow V, a doublet at the origin, double sources of strength $2Q$ placed symmetrically on the circular boundary with unit radius at angles $\pm\delta$, and their image sinks at the origin. This constitution satisfies the circular boundary[13], AS_1BS_2 of which the radius is 1. The radius 1 is different from that of Parkinson's R. The separation points are S_1 and S_2 of which angular coordinates are $\pm\alpha$. The separated streamlines start normally from the circular boundary[13]. The complex potential and the complex velocity are,

$$W(\zeta) = V\left(\zeta + \frac{1}{\zeta}\right) + \frac{Q}{\pi}\left\{\ln\left(\zeta - e^{i\delta}\right) + \ln\left(\zeta - e^{-i\delta}\right) - \ln\zeta\right\}, \quad \cdots (2.1.1)$$

and,

$$\frac{dW}{d\zeta}(\zeta) = V\left(1 - \frac{1}{\zeta^2}\right) + \frac{Q}{\pi}\left(\frac{1}{\zeta - e^{i\delta}} + \frac{1}{\zeta - e^{-i\delta}} - \frac{1}{\zeta}\right), \quad \cdots (2.1.2)$$

respectively.

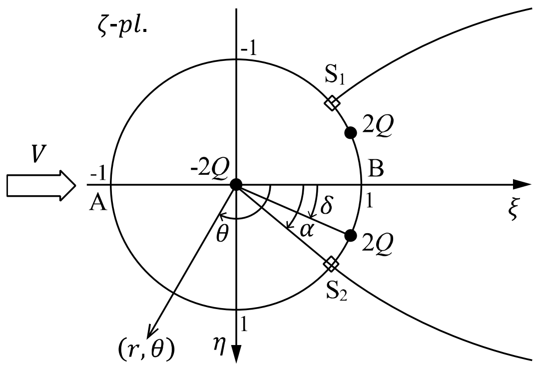

Fig. 2.1.1 Basic transform plane, ζ-pl.

The complex velocity on the circle AS_1BS_2 is,

$$\begin{aligned}\left.\frac{dW}{d\zeta}\right|_{r=1} &= V\left(1-e^{-2i\theta}\right)+\frac{Q}{\pi}\left(\frac{1}{e^{i\theta}-e^{i\delta}}+\frac{1}{e^{i\theta}-e^{-i\delta}}-e^{-i\theta}\right)\\ &= 2Vie^{-i\theta}\sin\theta+\frac{Q}{\pi}\frac{i\sin\theta}{2e^{i\theta}(\cos\theta-\cos\delta)}\\ &= 2ie^{-i\theta}\sin\theta\left(V+\frac{Q}{2\pi}\frac{1}{\cos\theta-\cos\delta}\right), \quad \ldots(2.1.3)\end{aligned}$$

and the velocity is,

$$\left|\frac{dW}{d\zeta}\right|_{r=1}=2\sin\theta\left(V+\frac{Q}{2\pi}\frac{1}{\cos\theta-\cos\delta}\right). \quad \ldots(2.1.4)$$

The separation points S_1 and S_2, *s.p.*, satisfies,

$$\left.\frac{dW}{d\zeta}\right|_{s.p.}=2ie^{\mp i\alpha}\sin\theta\left(V+\frac{Q}{2\pi}\frac{1}{\cos\alpha-\cos\delta}\right)=0. \quad \cdots(2.1.5)$$

Therefore,

$$Q=2\pi V(\cos\delta-\cos\alpha). \quad \cdots(2.1.6)$$

Equation (2.1.1) in terms of ξ and η is,

$$\begin{aligned}W &= V\left\{\left(\xi+\frac{\xi}{\xi^2+\eta^2}\right)+i\left(\eta-\frac{\eta}{\xi^2+\eta^2}\right)\right\}\\ &\quad+\frac{Q}{\pi}\left[\ln\left\{\frac{\sqrt{(\xi-\cos\delta)^2+(\eta-\sin\delta)^2}\sqrt{(\xi-\cos\delta)^2+(\eta+\sin\delta)^2}}{\sqrt{\xi^2+\eta^2}}\right\}\right.\\ &\quad\left.+i\left(\tan^{-1}\frac{\eta-\sin\delta}{\xi-\cos\delta}+\tan^{-1}\frac{\eta+\sin\delta}{\xi-\cos\delta}-\tan^{-1}\frac{\eta}{\xi}\right)\right]\end{aligned}$$

$$= V\xi\left(1+\frac{1}{\xi^2+\eta^2}\right)+\frac{Q}{\pi}\ln\left\{\frac{\sqrt{(\xi-\cos\delta)^2+(\eta-\sin\delta)^2}\sqrt{(\xi-\cos\delta)^2+(\eta+\sin\delta)^2}}{\sqrt{\xi^2+\eta^2}}\right\}$$

$$+i\left\{V\eta\left(1-\frac{1}{\xi^2+\eta^2}\right)+\frac{Q}{\pi}\left(\tan^{-1}\frac{\eta-\sin\delta}{\xi-\cos\delta}+\tan^{-1}\frac{\eta+\sin\delta}{\xi-\cos\delta}-\tan^{-1}\frac{\eta}{\xi}\right)\right\}. \quad \cdots (2.1.7)$$

Therefore, the streamline function Ψ is,

$$\Psi = V\eta\left(1-\frac{1}{\xi^2+\eta^2}\right)+\frac{Q}{\pi}\left(\tan^{-1}\frac{\eta-\sin\delta}{\xi-\cos\delta}+\tan^{-1}\frac{\eta+\sin\delta}{\xi-\cos\delta}-\tan^{-1}\frac{\eta}{\xi}\right)$$
$$= Vr\sin\theta\left(1-\frac{1}{r^2}\right)+\frac{Q}{\pi}\left(\tan^{-1}\frac{r\sin\theta-\sin\delta}{r\cos\theta-\cos\delta}+\tan^{-1}\frac{r\sin\theta+\sin\delta}{r\cos\theta-\cos\delta}-\theta\right). \quad \cdots (2.1.8)$$

Note that the following equation determines the coordinates of the separated streamline in the ζ-pl. and that Q/V given by Eq. (2.1.6) tells the depth of the separated streamline from the axis of symmetry, ξ-axis[13].

$$\Psi = \pm Q. \quad \cdots (2.1.9)$$

2.1.2 Transformation to separated flow around circular cylinders

Let us consider the separated flow around circular cylinders of which the radius is 1 and the center is at the origin. The radius and the location of the center are different from Parkinson and Jandali[13].

Before considering such flows, consider the separated flow around a cylinder with the radius $\widetilde{r_0}'$ of which center is at the origin in the $\widetilde{\zeta}'$-pl. as shown Fig. 2.1.2. Variables ($\widetilde{r}'$, $\widetilde{\theta}'$) represent polar coordinates of an arbitrary point. As Parkinson and Jandali[13] did, the Joukowsky transformation relates the circular boundary, AS_1BS_2 in the ζ-pl., to the slit AS_1BS_2 in the $\widetilde{\zeta}'$-pl. The cylinder AS_1DS_2 assumes a circular cylinder in the $\widetilde{\zeta}'$-pl. on which the flow separates at S_1 and S_2 of which angular coordinates are $\pm\widetilde{\theta_s}'$. The transformation is,

$$\widetilde{\zeta}' = \zeta-\cos\alpha-\frac{\sin^2\alpha}{\zeta-\cos\alpha}-e. \quad \cdots (2.1.10)$$

The variable e in Eq. (2.1.10) is an offset placing the center of the cylinder AS_1DS_2 at the origin as shown in Fig. 2.1.2.

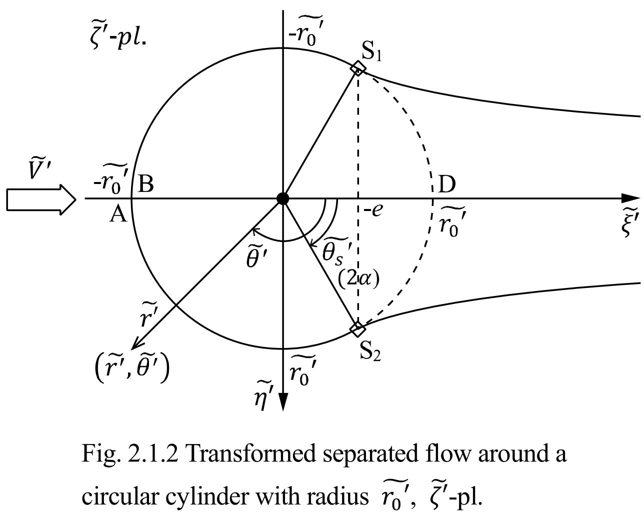

Fig. 2.1.2 Transformed separated flow around a circular cylinder with radius $\widetilde{r_0}'$, $\widetilde{\zeta}'$-pl.

The separated streamlines at S_1 and S_2 are normal to the circular boundary[13] in the ζ-pl. Since the angles at S_1 and S_2, the critical points, are doubled by the Joukowsky transformation, the separated streamlines are tangential to the cylinder AS_1DS_2 in the $\widetilde{\zeta}'$-pl. Therefore, the separation angle, $\widetilde{\theta_s}'$, in the $\widetilde{\zeta}'$-pl. is,

$$\widetilde{\theta_s}' = 2\alpha. \qquad \cdots (2.1.11)$$

The basic characteristics of Joukowsky transformation tell that *e* in Eq. (2.1.10) is,

$$e = 2\sin\alpha\tan\left\{\frac{\pi}{2} - \left(\pi - \widetilde{\theta_s}'\right)\right\} = 2\sin\alpha\tan\left\{\frac{\pi}{2} - (\pi - 2\alpha)\right\} = -\frac{2\sin\alpha}{\tan 2\alpha} = \frac{1}{\cos\alpha} - 2\cos\alpha. \qquad \cdots (2.1.12)$$

Therefore, the transformation from the ζ-pl., to the $\widetilde{\zeta}'$-pl. is,

$$\widetilde{\zeta}' = \zeta - \cos\alpha - \frac{\sin^2\alpha}{\zeta - \cos\alpha} - \frac{1}{\cos\alpha} + 2\cos\alpha. \qquad \cdots (2.1.13)$$

The radius of the cylinder AS_1DS_2, $\widetilde{r_0}'$, in the $\widetilde{\zeta}'$-pl. is,

$$\widetilde{r_0}' = \frac{2\sin\alpha}{\sin\left(\pi - \widetilde{\theta_s}'\right)} = \frac{2\sin\alpha}{\sin(\pi - 2\alpha)} = \frac{1}{\cos\alpha}. \qquad \cdots (2.1.14)$$

Accordingly, the transformation from the ζ-pl. to the $\tilde{\zeta}$-pl. shown in Fig. 2.1.3 representing the separated flow around a circular cylinder of which the radius is 1 and the center is at the origin is,

$$\begin{aligned}\tilde{\zeta} &= \frac{1}{\widetilde{\widetilde{r_0}'}}\widetilde{\zeta}' = \frac{1}{\widetilde{\widetilde{r_0}'}}\left(\zeta - \cos\alpha - \frac{\sin^2\alpha}{\zeta - \cos\alpha} - \frac{1}{\cos\alpha} + 2\cos\alpha\right) \\ &= \left(\zeta - \cos\alpha - \frac{\sin^2\alpha}{\zeta - \cos\alpha}\right)\cos\alpha + \cos 2\alpha. \qquad \cdots (2.1.15)\end{aligned}$$

Variables $(\tilde{r},\ \tilde{\theta})$ and $(\tilde{\xi},\ \tilde{\eta})$ in the $\tilde{\zeta}$-pl. represent polar and orthogonal coordinates of an arbitrary point, respectively. Equation (2.1.15) also transforms the coordinates of the separated streamline in the ζ-pl. defined by Eq. (2.1.9) to those in the $\tilde{\zeta}$-pl.

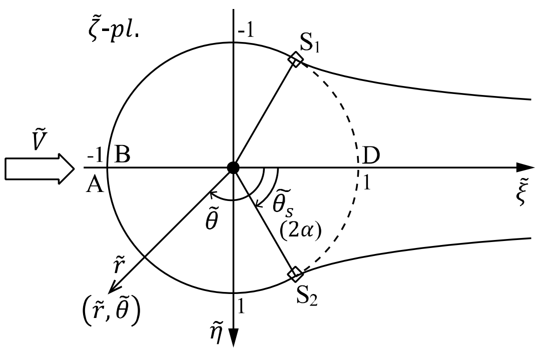

Fig. 2.1.3 Transformed separated flow around a circular cylinder with radius 1, $\tilde{\zeta}$-pl.

Equation (2.1.15) preserves the angles between the $\tilde{\zeta}'$-pl. and the $\tilde{\zeta}$-pl. Substituting the condition at the separation points, *s.p.*, in the ζ-pl.;

$$\zeta|_{s.p.} = e^{\pm i\alpha}, \quad \cdots (2.1.16)$$

into Eq. (2.1.15) confirms Eq. (2.1.11) as,

$$\tilde{\zeta}\Big|_{s.p.} = e^{\pm 2i\alpha}. \quad \cdots (2.1.17)$$

Therefore, the separation angle, $\tilde{\theta_s}$, in the $\tilde{\zeta}$-pl. is,

$$\tilde{\theta_s} = 2\alpha. \quad \cdots (2.1.18)$$

The $\tilde{\zeta}$-pl. is the intermediate plane relating the basic transform plane, the ζ-pl., to the physical plane described later.

2.1.3 Relations of the separated flow around a cylinder to the basic transform plane

Differentiation of Eq. (2.1.15) is,

$$\frac{d\tilde{\zeta}}{d\zeta} = \left\{1 + \frac{\sin^2\alpha}{(\zeta - \cos\alpha)^2}\right\}\cos\alpha. \quad \cdots (2.1.19)$$

Therefore, the complex velocity in the $\tilde{\zeta}$-pl. is,

$$\frac{dW}{d\tilde{\zeta}} = \frac{dW/d\zeta}{d\tilde{\zeta}/d\zeta} = \frac{dW}{d\zeta}\frac{1}{\{1 + \sin^2\alpha/(\zeta - \cos\alpha)^2\}\cos\alpha}. \quad \cdots (2.1.20)$$

Since,

$$\left.\frac{d\tilde{\zeta}}{d\zeta}\right|_{\zeta,\tilde{\zeta}\to\infty} = \cos\alpha, \quad \cdots (2.1.21)$$

the relation between velocities of the uniform flow in the ζ-pl. and the $\tilde{\zeta}$-pl. is,

$$\tilde{V} = \frac{V}{\cos\alpha}. \quad \cdots (2.1.22)$$

Based on Eq. (2.1.15), $\tilde{\zeta}$ on the circular cylinder is,

$$\begin{aligned}\tilde{\zeta}\Big|_{r,\tilde{r}=1} &= \zeta\cos\alpha - \frac{\sin^2\alpha\cos\alpha}{\zeta - \cos\alpha} - \sin^2\alpha\Bigg|_{r=1}\\ &= \frac{2\cos\alpha\cos\theta\,(1 - \cos\alpha\cos\theta) - \sin^2\alpha}{1 + \cos^2\alpha - 2\cos\alpha\cos\theta} + i\frac{2\cos\alpha\cos\theta\,(1 - \cos\alpha\cos\theta)}{1 + \cos^2\alpha - 2\cos\alpha\cos\theta}. \quad \cdots (2.1.23)\end{aligned}$$

Therefore, the relation between θ in the ζ-pl. and $\tilde{\theta}$ in the $\tilde{\zeta}$-pl. where r and $\tilde{r}$ are both equal to 1 is,

$$\tilde{\theta}\Big|_{r,\tilde{r}=1} = \tan^{-1}\left\{1 + \frac{\sin^2\alpha}{2\cos\alpha\cos\theta\,(1-\cos\alpha\cos\theta) - \sin^2\alpha}\right\}$$
$$= \cos^{-1}\frac{2\cos\alpha\cos\theta\,(1-\cos\alpha\cos\theta) - \sin^2\alpha}{1+\cos^2\alpha - 2\cos\alpha\cos\theta}. \quad \cdots (2.1.24)$$

Since Eq. (2.1.19) on the circular cylinder is,

$$\left.\frac{d\tilde{\zeta}}{d\zeta}\right|_{r=1} = \left\{1 + \frac{\sin^2\alpha}{(e^{i\theta}-\cos\alpha)^2}\right\}\cos\alpha$$
$$= \frac{2(\cos\theta - \cos\alpha)e^{i\theta}}{\{(\cos\theta-\cos\alpha) + i\sin\theta\}^2}\cos\alpha, \quad \cdots (2.1.25)$$

$$\left|\frac{d\tilde{\zeta}}{d\zeta}\right|_{r=1} = \frac{2\cos\alpha\,(\cos\theta-\cos\alpha)}{(\cos\theta-\cos\alpha)^2+\sin^2\theta} = \frac{2\cos\alpha\,(\cos\theta-\cos\alpha)}{1+\cos^2\alpha-2\cos\alpha\cos\theta}. \quad \cdots (2.1.26)$$

For the separation point, *s.p.*, where θ is equal to $\pm\alpha$, Eq. (2.1.26) is,

$$\left.\frac{d\tilde{\zeta}}{d\zeta}\right|_{s.p.} = 0. \quad \cdots (2.1.27)$$

Equation (2.1.27) confirms that the separation points are the critical points.

2.2 Separated flow around ship cross-sections

2.2.1 Transformation to ship cross-sections

The physical plane, *z*-pl., shown in Fig. 2.2.1 represents a separated flow around a ship cross-section with its mirror image in unbounded uniform flow. Variables (R, Θ) and (x, y) represent polar and orthogonal coordinates of an arbitrary point, respectively. B_r and d stand for the breadth and the drought, respectively. The separation angles are $\pm\Theta_s$.

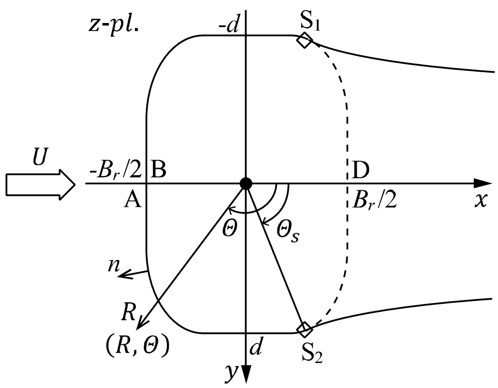

Fig. 2.2.1 Physical plane, z-pl.

Lewis form approximation[14] defined by,

$$z = M\left(\tilde{\zeta} + \frac{C_1}{\tilde{\zeta}} + \frac{C_3}{\tilde{\zeta}^3}\right), \quad \cdots (2.2.1)$$

transforms a circle of which radius is equal to 1 to a shape approximating a ship cross-section. The area of a ship cross-section, B_r and d determine M, C_1, and C_2. This study employs Eq. (2.2.1) to transform the flow field in the $\tilde{\zeta}$-pl. to that in the z-pl.

Let us consider in the $\tilde{\zeta}$-pl. a point on the circular cylinder of the radius, $\tilde{r}$, is equal to 1. The point corresponds to a point on the surface of a ship cross-section in the z-pl. Substituting,

$$\tilde{\zeta} = e^{i\tilde{\theta}}, \quad \cdots (2.2.2)$$

into Eq. (2.2.1) leads to,

$$z = M\{(1 + C_1)\cos\tilde{\theta} + C_3 \cos 3\tilde{\theta}\} + iM\{(1 - C_1)\sin\tilde{\theta} - C_3 \sin 3\tilde{\theta}\}, \quad \cdots (2.2.3)$$

and

$$x = M\{(1 + C_1)\cos\tilde{\theta} + C_3 \cos 3\tilde{\theta}\}, y = M\{(1 - C_1)\sin\tilde{\theta} - C_3 \sin 3\tilde{\theta}\}. \quad \cdots (2.2.4)$$

Therefore, the relation between the angle $\tilde{\theta}$ on the circular cylinder in the $\tilde{\zeta}$-pl. and that on the surface of the ship cross-section Θ in the z-pl. is,

$$\begin{aligned}\Theta &= \tan^{-1}\frac{(1 - C_1)\sin\tilde{\theta} - C_3 \sin 3\tilde{\theta}}{(1 + C_1)\cos\tilde{\theta} + C_3 \cos 3\tilde{\theta}} \\ &= \cos^{-1}\frac{(1 + C_1)\cos\tilde{\theta} + C_3 \cos 3\tilde{\theta}}{\sqrt{1 + {C_1}^2 + {C_3}^2 + 2C_1(1 + C_3)\cos 2\tilde{\theta} + 2C_3 \cos 4\tilde{\theta}}} \\ &= \cos^{-1}\frac{\{1 + C_1 - C_3(3 - 4\cos^2\tilde{\theta})\}\cos\tilde{\theta}}{\sqrt{(C_1 - C_3 - 1)^2 + 4(C_1 + C_1C_3 - 4C_3)\cos^2\tilde{\theta} + 16C_3\cos^4\tilde{\theta}}}. \quad \cdots (2.2.5)\end{aligned}$$

Substituting Eq. (2.1.18) into Eq. (2.2.5) leads to the relation between the separation point angle in the z-pl., Θ_s, and α in the ζ-pl. as,

$$\begin{aligned}\Theta_s &= \tan^{-1}\frac{(1 - C_1)\sin 2\alpha - C_3 \sin 6\alpha}{(1 + C_1)\cos 2\alpha + C_3 \cos 6\alpha} \\ &= \cos^{-1}\frac{(1 + C_1)\cos 2\alpha + C_3 \cos 6\alpha}{\sqrt{1 + {C_1}^2 + {C_3}^2 + 2C_1(1 + C_3)\cos 4\alpha + 2C_3 \cos 8\alpha}}. \quad \cdots (2.2.6)\end{aligned}$$

Equation (2.2.6) determines α, though implicitly, using given separation angle Θ_s in the z-pl. This means that α is a function of Θ_s, $\alpha(\Theta_s)$.

Differentiation of Eq. (2.2.1) is,

$$\frac{dz}{d\tilde{\zeta}} = M\left(1 - \frac{C_1}{\tilde{\zeta}^2} - \frac{3C_3}{\tilde{\zeta}^4}\right). \quad \cdots (2.2.7)$$

Therefore, the complex velocity in the z-pl. is,

$$\frac{dW}{dz} = \frac{dW/d\tilde{\zeta}}{dz/d\tilde{\zeta}} = \frac{dW}{d\tilde{\zeta}} \frac{1}{M\left(1 - C_1/\tilde{\zeta}^2 - 3C_3/\tilde{\zeta}^4\right)}. \quad \cdots (2.2.8)$$

Since,

$$\left.\frac{dz}{d\tilde{\zeta}}\right|_{\tilde{\zeta}, z \to \infty} = M, \quad \cdots (2.2.9)$$

the relation between velocities of the uniform flow in the $\tilde{\zeta}$-pl. and the z-pl. is,

$$U = \frac{\tilde{V}}{M}. \quad \cdots (2.2.10)$$

Substituting Eq. (2.1.22) into Eq. (2.2.10) leads to,

$$V = (M \cos\alpha)U. \quad \cdots (2.2.11)$$

Equation (2.2.11) determines V in the ζ-pl. using U and α. Since Θ_s determines α by Eq. (2.2.6), V is a function of U and Θ_s, $V(U, \Theta_s)$.

Substituting Eq. (2.2.11) into Eq. (2.1.6) leads to,

$$Q = 2\pi MU(\cos\delta - \cos\alpha)\cos\alpha. \quad \cdots (2.2.12)$$

For further analysis, on the surface of a ship cross-sections in the z-pl. or on the surface of a circular cylinder in the $\tilde{\zeta}$-pl.,

$$\left.\frac{dz}{d\tilde{\zeta}}\right|_{\tilde{r}=1} = M\left\{\left(1 - C_1\cos 2\tilde{\theta} - 3C_3\cos 4\tilde{\theta}\right) + i\left(C_1 \sin 2\tilde{\theta} + 3C_3 \sin 4\tilde{\theta}\right)\right\}. \quad \cdots (2.2.13)$$

and, therefore,

$$\left|\frac{dz}{d\tilde{\zeta}}\right|_{\tilde{r}=1} = M\sqrt{1 + {C_1}^2 + 9{C_3}^2 - 2C_1(1 - 3C_3)\cos 2\tilde{\theta} - 6C_3\cos 4\tilde{\theta}}. \quad \cdots (2.2.14)$$

Note that Eq. (2.2.1) also transforms the coordinates of the separated streamline and that Q/U given by Eq. (2.2.12) tells the depth of the separated streamline from the axis of symmetry, x-axis in the z-pl. [13)]

2.2.2 Pressure and drag coefficient

Let us consider the pressure at separation points in the z-pl. Bernoulli's theorem;

$$p + \frac{1}{2}\rho\left|\frac{dW}{dz}\right|^2 = p_\infty + \frac{1}{2}\rho U^2, \quad \cdots (2.2.15)$$

defines the pressure coefficient, C_p in the z-pl. as,

$$C_p = \frac{p - p_\infty}{\rho U^2/2} = 1 - \left|\frac{dW}{dz}\right|^2 / U^2, \quad \cdots (2.2.16)$$

where p and p_∞ are the pressure at a point and infinity in the z-pl., respectively, and ρ is the density of water.

The complex velocity in the z-pl. is,

$$\frac{dW}{dz} = \frac{dW/d\tilde{\zeta}}{dz/d\tilde{\zeta}} = \frac{dW/d\zeta}{d\tilde{\zeta}/d\zeta}\frac{1}{dz/d\tilde{\zeta}}. \quad \cdots (2.2.17)$$

Since Eqs. (2.1.5) and (2.1.27) hold at the separation points,

$$\left.\frac{dW}{d\tilde{\zeta}}\right|_{s.p,} = \frac{0}{0}. \quad \cdots (2.2.18)$$

Equations (2.2.16) through (2.2.18), and Eq. (2.2.13) suggest that $dW/dz|_{s.p.}$ and C_p at the separation points are also indefinite.

Since the velocity dW/dz at separation points should be finite in the z-pl., the introduction of the base pressure p_b and its coefficient C_{pb} defines $|dW/dz|_{s.p.}$ as,

$$C_{pb} = \frac{p_b - p_\infty}{\rho U^2/2} = 1 - \left|\frac{dW}{dz}\right|_{s.p.}^2 / U^2. \quad \cdots (2.2.19)$$

Let us assume that the pressure over the downstream surface of a ship cross-section, S_1DS_2, is constant p_b and ignore the flow inside the separation streamlines as in Parkinson and Jandali[13]. The pressure coefficient on the downstream surface in the lower half of the z-pl. is,

$$C_{p(\theta)} = C_{pb} \quad (0 \le \theta \le \alpha \; or \; 0 \le \Theta \le \Theta_s), \quad \cdots (2.2.20)$$

Substituting Eqs. (2.2.11) and (2.2.12) into Eq. (2.1.4) leads to,

$$\left|\frac{dW}{d\zeta}\right|_{sur.} = \left|\frac{dW}{d\zeta}\right|_{r=1} = 2MU\cos\alpha\sin\theta\frac{\cos\theta - \cos\alpha}{\cos\theta - \cos\delta}. \quad ... (2.2.21)$$

Using Eqs. (2.2.21) and (2.1.26) leads to,

$$\frac{|dW/d\zeta|_{sur.}}{|d\tilde{\zeta}/d\zeta|_{sur.}} = \frac{|dW/d\zeta|_{r=1}}{|d\tilde{\zeta}/d\zeta|_{r=1}} = MU\sin\theta\frac{1 + \cos^2\alpha - 2\cos\alpha\cos\theta}{\cos\theta - \cos\delta}. \quad \cdots (2.2.22)$$

Using Eqs. (2.2.22) and (2.2.14) leads to,

$$\left|\frac{dW}{dz}\right|_{sur.} = \frac{|dW/d\zeta|_{r=1}}{|d\tilde{\zeta}/d\zeta|_{r=1}}\frac{1}{|dz/d\tilde{\zeta}|_{\tilde{r}=1}}$$

$$= \frac{U(1+\cos^2\alpha - 2\cos\alpha\cos\theta)\sin\theta}{(\cos\theta-\cos\delta)\sqrt{1+{C_1}^2+9{C_3}^2-2C_1(1-3C_3)\cos 2\tilde{\theta}-6C_3\cos 4\tilde{\theta}}}. \quad \cdots (2.2.23)$$

Therefore, Eq. (2.2.16) with Eq. (2.2.23) tells C_p, as a function of θ, on the upstream surface in the lower half of the z-pl. as,

$$\begin{aligned} C_{p(\theta)} &= 1 - \frac{(1+\cos^2\alpha-2\cos\alpha\cos\theta)^2\sin^2\theta}{(\cos\theta-\cos\delta)^2\left\{1+{C_1}^2+9{C_3}^2-2C_1(1-3C_3)\cos 2\tilde{\theta}_{(\theta)}-6C_3\cos 4\tilde{\theta}_{(\theta)}\right\}} \\ &= 1 - \frac{(1+\cos^2\alpha-2\cos\alpha\cos\theta)^2\sin^2\theta}{(\cos\theta-\cos\delta)^2\left\{(1+C_1-3C_3)^2-4(C_1-12C_3-3C_1C_3)\cos^2\tilde{\theta}_{(\theta)}-48C_3\cos^4\tilde{\theta}_{(\theta)}\right\}}, \\ & \qquad (\alpha \le \theta \le \pi \ or\ \Theta_s \le \theta \le \pi), \quad \cdots (2.2.24) \end{aligned}$$

where $\tilde{\theta}$ in the denominator is also a function of θ as shown in Eq. (2.1.24).

Since C_p is equal to C_{pb} at the separation point, substituting α into θ and Eq. (2.1.18) into $\tilde{\theta}$ lead Eq. (2.2.24) to,

$$C_{pb} = 1 - \frac{\sin^6\alpha}{(\cos\alpha-\cos\delta)^2\left\{1+{C_1}^2+9{C_3}^2-2C_1(1-3C_3)\cos 4\alpha-6C_3\cos 8\alpha\right\}}. \quad \cdots (2.2.25)$$

Since,

$$0 \le 1 - C_p, \quad \cdots (2.2.26)$$

Equation (2.2.25) tells,

$$0 \le 1+{C_1}^2+9{C_3}^2-2C_1(1-3C_3)\cos 2\tilde{\theta}-6C_3\cos 4\tilde{\theta}. \quad \cdots (2.2.27)$$

Also since,

$$\delta \le \alpha \le \pi, \quad \cdots (2.2.28)$$

$$\cos\alpha - \cos\delta \le 0. \quad \cdots (2.2.29)$$

Therefore,

$$\delta = \cos^{-1}\left[\cos\alpha + \frac{\sin^3\alpha}{\sqrt{(1-C_{pb})\left\{1+{C_1}^2+9{C_3}^2-2C_1(1-3C_3)\cos 4\alpha-6C_3\cos 8\alpha\right\}}}\right]. \quad \cdots (2.2.30)$$

Equations (2.2.30) determine δ using given C_{pb}, and α. Since Θ_s determines α by Eq. (2.2.6), δ is a function of Θ_s, and C_{pb}, $\delta(\Theta_s, C_{pb})$. Since δ, α and U determine Q by Eq. (2.2.12), Q is a function of U, Θ_s and C_{pb}, $Q(U, \Theta_s, C_{pb})$. Now, U, Θ_s, and C_{pb} in the z-pl. determine all the parameters, $\alpha(\Theta_s)$, $\delta(\Theta_s, C_{pb})$, $V(U, \Theta_s)$, $Q(U, \Theta_s, C_{pb})$ in the ζ-pl. Figure 2.2.2 explains how the variables in the z-pl. determine those in the ζ-pl.

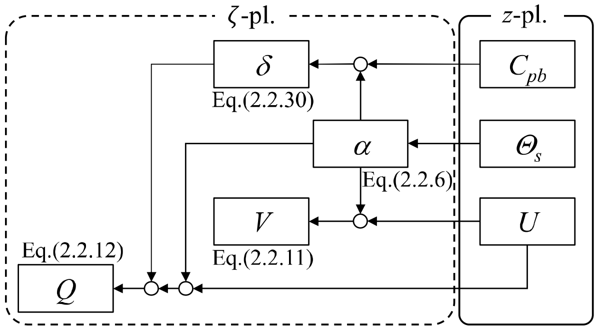

Fig. 2.2.2 Relation between variables in the z-pl. and those in the ζ-pl. for the wake source model.

The drag coefficient of a ship cross-section is defined by,

$$C_d = -\frac{1}{\rho U^2(2d)/2}\oint pds\cos\widehat{nx} = -\frac{1}{\rho U^2(2d)/2}\oint pds\frac{dy}{ds} = -\frac{1}{\rho U^2 d/2}\int pdy = -\frac{1}{d}\int C_p dy$$
$$= -\frac{1}{d}\left(C_{pb}y_s + \int_\alpha^\pi C_p\frac{dy}{d\tilde{\theta}}\frac{d\tilde{\theta}}{d\theta}d\theta\right), \quad \cdots(2.2.31)$$

where ds and $\widehat{nx}$ are a line segment along the surface of a ship cross-section and the angle of a normal outward vector on the surface to the positive direction of the x-axis. The coordinates (x_s, $\pm y_s$) stand for the separation points.

Equation (2.2.4) using Eq. (2.1.18) at separation points tells,

$$y_s = M\{(1-C_1)\sin 2\alpha - C_3\sin 6\alpha\}. \quad \cdots(2.2.32)$$

Differentiating Eqs. (2.2.4) and (2.1.24) leads to,

$$\frac{dy}{d\tilde{\theta}} = M\{(1-C_1)\cos\tilde{\theta} - 3C_3\cos 3\tilde{\theta}\}$$
$$= M\{1 - C_1 + 3C_3(3-4\cos^2\tilde{\theta})\}\cos\tilde{\theta}. \quad \cdots(2.2.33)$$

and,

$$\left.\frac{d\tilde{\theta}}{d\theta}\right|_{r,\tilde{r}=1} = \frac{2\cos\alpha(\cos\alpha - \cos\theta)}{1+\cos\alpha(\cos\alpha - 2\cos\theta)}. \quad \cdots(2.2.34)$$

Equation (2.2.31) with Eqs. (2.2.24), and Eqs. (2.2.32) through (2.2.34) calculate the drag coefficient C_d of a ship cross-sections.

2.2.3 Condition for the separated streamline

Parkinson and Jandali[13] noted based on the discussion by Woods[16] that the separated streamline of the circular cylinder in order not to intersect the cylinder surface must satisfy at the separation point,

$$\frac{2}{3}\sqrt{1-\widetilde{C_{pb}}} \le \sin(\pi - \widetilde{\theta_s}) = \sin\widetilde{\theta_s}, \quad \cdots(2.2.35)$$

where $\widetilde{C_{pb}}$ is the base pressure coefficient for the separated flow around a circular cylinder. The following equation defines $\widetilde{C_{pb}}$.

$$\widetilde{C_{pb}} = \frac{\widetilde{p_b} - \widetilde{p_\infty}}{\rho \tilde{V}^2/2} = 1 - \left|\frac{dW}{d\tilde{\zeta}}\right|_{s.p.}^2 / \tilde{V}^2, \quad \cdots (2.2.36)$$

where $\widetilde{p_b}$ and $\widetilde{p_\infty}$ are the pressure at a point and infinity in the $\tilde{\zeta}$-pl., respectively. $\widetilde{C_{pb}}$ defines $dW/d\check{\zeta}\big|_{s.p.}$ that is indefinite as in Eq. (2.2.18). Equation (2.2.19) with Eq. (2.2.10) tells,

$$1 - C_{pb} = \left|\frac{dW}{dz}\right|_{s.p.}^2 \frac{1}{U^2} = \left|\frac{dW}{d\tilde{\zeta}}\right|_{s.p.}^2 \frac{1}{\tilde{V}^2} \frac{1}{\left|\frac{dz}{d\tilde{\zeta}}\right|_{s.p.}^2} \frac{\tilde{V}^2}{U^2} = \left(1 - \widetilde{C_{pb}}\right) \frac{1}{\left|\frac{dz}{d\tilde{\zeta}}\right|_{s.p.}^2} M^2. \quad \cdots (2.2.37)$$

Substituting Eq. (2.2.37) into Eq. (2.2.35) using Eq. (2.1.18) leads to,

$$\frac{2}{3} \frac{1}{M} \left|\frac{dz}{d\tilde{\zeta}}\right|_{s.p.} \sqrt{1 - C_{pb}} \leq \sin \widetilde{\theta_s}. \quad \cdots (2.2.38)$$

Substituting Eq. (2.2.14) into Eq. (2.2.38) using Eq. (2.1.18) leads to,

$$\begin{aligned} \frac{2}{3}\sqrt{1 - C_{pb}} &\leq \frac{\sin \widetilde{\theta_s}}{\sqrt{1 + {C_1}^2 + 9{C_3}^2 - 2C_1(1 - 3C_3)\cos 2\widetilde{\theta_s} - 6C_3 \cos 4\widetilde{\theta_s}}} \\ &\leq \frac{\sin 2\alpha}{\sqrt{1 + {C_1}^2 + 9{C_3}^2 - 2C_1(1 - 3C_3)\cos 4\alpha - 6C_3 \cos 8\alpha}}, \quad \cdots (2.2.39) \end{aligned}$$

Equation (2.2.39) for the z-pl. corresponds to Eq. (2.2.35) for the $\tilde{\zeta}$-pl.

Following is another line of thought leading to Eq. (2.2.39). Since both C_1 and C_3 are zero for circular cylinders in the z-pl., Equation (2.2.25) suggests,

$$\widetilde{C_{pb}} = 1 - \frac{\sin^6 \alpha}{(\cos \alpha - \cos \delta)^2}. \quad \cdots (2.2.40)$$

Substituting Eq. (2.2.40) into Eq. (2.2.35) leads to,

$$\frac{2}{3} \frac{\sin^3 \alpha}{\cos \delta - \cos \alpha} \leq \sin \widetilde{\theta_s}. \quad \cdots (2.2.41)$$

Substituting Eq. (2.2.30) into Eq. (2.2.41) also leads to Eq. (2.2.39).

Modifying Eq. (2.2.39) leads to,

$$C_{pb} \geq 1 - \frac{9}{4}\frac{\sin^2 2\alpha}{\left\{1 + {C_1}^2 + 9{C_3}^2 - 2C_1(1 - 3C_3)\cos 4\alpha - 6C_3 \cos 8\alpha\right\}}. \quad \cdots (2.2.42)$$

Since α is a function of Θ_s as shown in Eq. (2.2.6), C_{pb} has the minimum value defined by Eq. (2.2.42) for a given Θ_s .

Note that Eq. (2.2.42) or Eq. (2.2.39) means the physical requirement that the separated streamline does not intersect the surface of a ship cross-section in the z-pl., while Eq. (2.2.35) does so in the $\tilde{\zeta}$-pl. for circular cylinders.

3. Enhanced wake source model

The wake source model has two kinds of limitations. One comes from the physical requirement as explained in subsection 2.2.3. This chapter explains the other non-physical limitation of the wake source model and presents an enhanced wake source model that resolves the limitation.

3.1 Non-physical limitation of the wake source model

Equation (2.2.41) with Eq. (2.1.18) tells,

$$\begin{aligned}\cos\delta &\geq \cos\alpha + \frac{2}{3}\frac{\sin^3\alpha}{\sin 2\alpha} \\ &\geq \frac{1}{3}\left(2\cos\alpha + \frac{1}{\cos\alpha}\right). \quad \cdots (3.1.1)\end{aligned}$$

Let us consider a function f defined by,

$$f(\alpha) = \frac{1}{3}\left(2\cos\alpha + \frac{1}{\cos\alpha}\right), \quad \cdots (3.1.2)$$

and its derivative,

$$\frac{df}{d\alpha} = f'(\alpha) = -\frac{2}{3}\left(2 - \frac{1}{\cos^2\alpha}\right). \quad \cdots (3.1.3)$$

Equations (3.1.2) and (3.1.3) tell the properties of f as,

$$f(0) = 1, f\left(\frac{\pi}{4}\right) = \frac{2\sqrt{2}}{3}, f\left(\frac{\pi}{3}\right) = 1, f\left(\frac{\pi}{2}\right) = \infty, \quad \cdots (3.1.4)$$

and

$$f'(0) = 0, f'\left(\frac{\pi}{4}\right) = 0, \quad \cdots (3.1.5)$$

as shown in Fig. 3.1.1.

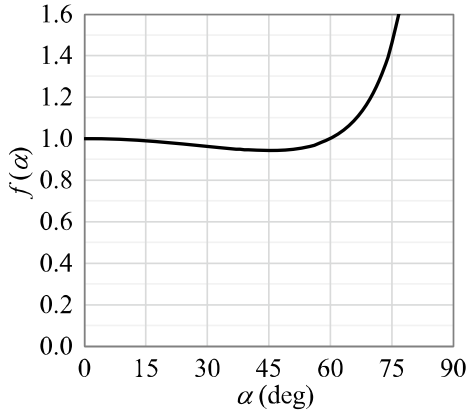

Fig. 3.1.1 $f(\alpha)$.

Equations (3.1.1) and (3.1.2), and the characteristics of f tell,

$$\cos\delta \geq f(\alpha) \geq f\left(\frac{\pi}{4}\right) = \frac{2\sqrt{2}}{3}, \quad \cdots (3.1.6)$$

and

$$\delta \leq \cos^{-1}\frac{2\sqrt{2}}{3} = 19.47\ (\mathrm{deg}). \quad \cdots (3.1.7)$$

Since,

$$\cos\delta \leq 1, \quad \cdots (3.1.8)$$

$$\alpha \leq \frac{\pi}{3}. \quad \cdots (3.1.9)$$

Substituting Eq. (2.2.30) into Eq. (3.1.8) leads to,

$$\frac{\sin^3\alpha}{\sqrt{(1-C_{pb})\{1+{C_1}^2+9{C_3}^2-2C_1(1-3C_3)\cos 4\alpha - 6C_3\cos 8\alpha\}}} \leq 1-\cos\alpha. \quad \cdots (3.1.10)$$

Therefore,

$$1-C_{pb} \geq \frac{\sin^6\alpha}{(1-\cos\alpha)^2\{1+{C_1}^2+9{C_3}^2-2C_1(1-3C_3)\cos 4\alpha - 6C_3\cos 8\alpha\}}. \quad \cdots (3.1.11)$$

or

$$C_{pb} \leq 1-\frac{\sin^6\alpha}{(1-\cos\alpha)^2\{1+{C_1}^2+9{C_3}^2-2C_1(1-3C_3)\cos 4\alpha - 6C_3\cos 8\alpha\}}. \quad \cdots (3.1.12)$$

Equation (3.1.12) or (3.1.11) is the non-physical limitation of the wake source model because Eq. (3.1.8) has no physical meaning.

Equation (3.1.9), also the non-physical limitation, defines the maximum value of Θ_s by Eq. (2.2.6) for a ship cross-section as,

$$\Theta_s \le \cos^{-1}\frac{(1+C_1)(-1/2)-C_3}{\sqrt{1+{C_1}^2+{C_3}^2+2C_1(1+C_3)(-1/2)+2C_3(-1/2)}}$$
$$\le \cos^{-1}\frac{-1-C_1+2C_3}{2\sqrt{1-C_1C_3+C_1(C_1-1)+C_3(C_3-1)}}. \quad \cdots (3.1.13)$$

3.2 C_{pb} range and examples for circular cylinders

Equations (3.1.12) and (2.2.42) define C_{pb} range for a ship cross-section as,

$$g_1(\alpha) \le C_{pb} \le g_2(\alpha), \quad \cdots (3.2.1)$$

where,

$$\begin{cases} g_1(\alpha) = 1 - \dfrac{9}{4}\dfrac{\sin^2 2\alpha}{\left\{1+{C_1}^2+9{C_3}^2-2C_1(1-3C_3)\cos 4\alpha - 6C_3\cos 8\alpha\right\}} \\ g_2(\alpha) = 1 - \dfrac{\sin^6\alpha}{(1-\cos\alpha)^2\left\{1+{C_1}^2+9{C_3}^2-2C_1(1-3C_3)\cos 4\alpha - 6C_3\cos 8\alpha\right\}} \end{cases}. \quad \cdots (3.2.2)$$

Let us consider the corresponding C_{pb} range for circular cylinders, $\widetilde{C_{pb}}$. Since both C_1 and C_3 are zero for circular cylinders,

$$\widetilde{g_1}(\alpha) \le \widetilde{C_{pb}} \le \widetilde{g_2}(\alpha), \quad \cdots (3.2.3)$$

where,

$$\begin{cases} \widetilde{g_1}(\alpha) = 1 - \dfrac{9}{4}\sin^2 2\alpha \\ \widetilde{g_2}(\alpha) = 1 - \dfrac{\sin^6\alpha}{(1-\cos\alpha)^2} \end{cases}. \quad \cdots (3.2.4)$$

The derivatives of $\widetilde{g_1}$ and $\widetilde{g_2}$ are,

$$\begin{cases} \widetilde{g_1}'(\alpha) = -9\sin 2\alpha\cos 2\alpha \\ \widetilde{g_2}'(\alpha) = -\dfrac{2(2\cos\alpha-1)\sin^5\alpha}{(1-\cos\alpha)^2} \end{cases}. \quad \cdots (3.2.5)$$

Equations (3.2.4) and (3.2.5) tell,

$$\begin{cases} \widetilde{g_1}(0) = 1, \widetilde{g_1}\left(\frac{\pi}{4}\right) = -\frac{5}{4}, \widetilde{g_1}\left(\frac{\pi}{3}\right) = -\frac{11}{16}, \widetilde{g_1}\left(\frac{\pi}{2}\right) = 1 \\ \widetilde{g_2}\left(\frac{\pi}{3}\right) = -\frac{11}{16}, \widetilde{g_2}\left(\frac{\pi}{2}\right) = 1 \end{cases}, \quad \cdots (3.2.6)$$

and

$$\begin{cases} \widetilde{g_1}'(0) = \widetilde{g_1}'\left(\frac{\pi}{4}\right) = \widetilde{g_1}'\left(\frac{\pi}{2}\right) = 0 \\ \widetilde{g_2}'\left(\frac{\pi}{3}\right) = \widetilde{g_2}'\left(\frac{\pi}{2}\right) = 0 \end{cases}, \quad \cdots (3.2.7)$$

respectively. Figure 3.2.1, based on Eqs. (3.2.6) and (3.2.7) shows characteristics of $\widetilde{g_1}$ and $\widetilde{g_2}$. Note that the abscissa α is equal to $\widetilde{\theta_s}/2$ for circular cylinders as in Eq. (2.1.18). Equation (3.1.13) for circular cylinders turns to,

$$\widetilde{\theta_s} \leq \cos^{-1}\left(-\frac{1}{2}\right) = \frac{2\pi}{3}. \quad \cdots (3.2.8)$$

Equation (3.1.12) is the result that comes from Eqs. (2.1.18) and (3.1.9) for circular cylinders. Equations (3.2.3) and (3.2.8) means in Fig. 3.2.1 that $\widetilde{C_{pb}}$ can have a value above the $\widetilde{g_1}$-line, below the $\widetilde{g_2}$-line and $\widetilde{\theta_s}/2$ equal to or less than π/3 where $\widetilde{g_1}$-line and $\widetilde{g_2}$-line lines intersect.

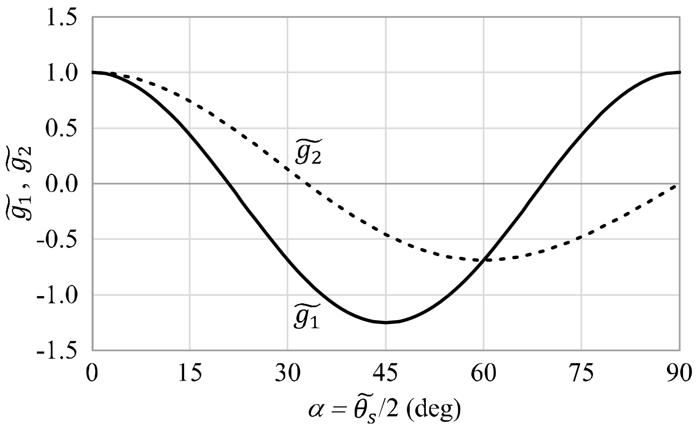

Fig. 3.2.1 $\widetilde{g_1}$ and $\widetilde{g_2}$.

The examples for the circular cylinder imply the non-physical limitation of Eqs. (3.1.12) and (3.1.13), the $\widetilde{g_2}$-line in Fig. 3.2.1, may prevent the wake source model to describe flow around ship cross-sections separating around the upstream bilge corner with relatively high pressure.

3.3 Enhanced wake source model for ship cross-sections

Let us introduce a flow model shown in Fig. 3.3.1 representing an alternative basic transform plane having an alternative complex potential for cases not satisfying Eq. (3.1.8). Let us call the alternative complex plane as the ζ_1-pl. though the same variables $(r,\ \theta)$ and $(\xi,\ \eta)$ and so forth are used as in the ζ-pl. The complex potential and the complex velocity are,

$$W(\zeta) = V\left(\zeta + \frac{1}{\zeta}\right) + \frac{Q}{\pi}\left\{\ln(\zeta - l) + \ln\left(\zeta - \frac{1}{l}\right) - \ln\zeta\right\}, \quad \cdots (3.3.1)$$

and,

$$\frac{dW}{d\zeta}(\zeta) = V\left(1 - \frac{1}{\zeta^2}\right) + \frac{Q}{\pi}\left(\frac{1}{\zeta - l} + \frac{1}{\zeta - 1/l} - \frac{1}{\zeta}\right), \quad \cdots (3.3.2)$$

respectively.

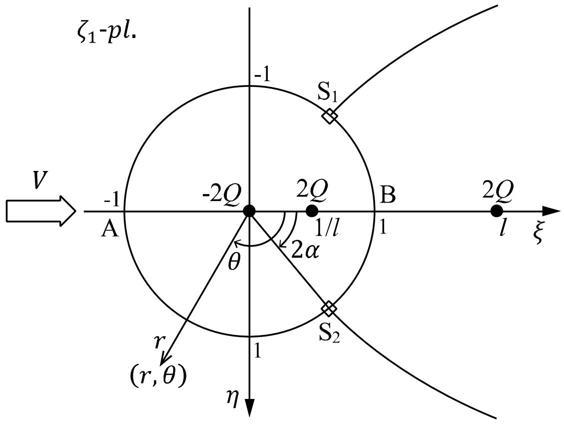

Fig. 3.3.1 Alternative complex plane, ζ_1-pl., for enhanced wake source model.

The complex velocity on the circle, AS_1BS_2, of which radius r is equal to 1 is,

$$\begin{aligned} \left.\frac{dW}{d\zeta}\right|_{r=1} &= V\left(1 - e^{-2i\theta}\right) + \frac{Q}{\pi}\left(\frac{1}{e^{i\theta} - l} + \frac{1}{e^{i\theta} - 1/l} - e^{-i\theta}\right) \\ &= 2Vie^{-i\theta}\sin\theta + \frac{Q}{\pi}\frac{2i\sin\theta}{e^{2i\theta} - (l + 1/l)e^{i\theta} + 1} \\ &= 2Vie^{-i\theta}\sin\theta + \frac{Q}{\pi}\frac{2ie^{-i\theta}\sin\theta}{e^{i\theta} - (l + 1/l) + e^{-i\theta}} \\ &= 2ie^{-i\theta}\sin\theta\left(V + \frac{Q}{2\pi}\frac{1}{\cos\theta - l^*}\right), \quad \ldots (3.3.3) \end{aligned}$$

where,

$$l^* = \frac{1}{2}\left(l + \frac{1}{l}\right). \quad \ldots (3.3.4)$$

The velocity on the circle is,

$$\left|\frac{dW}{d\zeta}\right|_{r=1} = 2\sin\theta\left(V + \frac{Q}{2\pi}\frac{1}{\cos\theta - l^*}\right). \quad \ldots (3.3.5)$$

The separation points S_1 and S_2, *s.p.*, satisfies,

$$\left.\frac{dW}{d\zeta}\right|_{s.p.} = 2ie^{\mp i\alpha}\sin\theta\left(V + \frac{Q}{2\pi}\frac{1}{\cos\alpha - l^*}\right) = 0. \quad \cdots (3.3.6)$$

Therefore,

$$Q = 2\pi V(l^* - \cos\alpha). \quad \cdots (3.3.7)$$

Equation (3.3.1) in terms of ξ and η in Fig. 3.3.1 is,

$$\begin{aligned}
W &= V\left\{\left(\xi + \frac{\xi}{\xi^2+\eta^2}\right) + i\left(\eta - \frac{\eta}{\xi^2+\eta^2}\right)\right\} \\
&\quad + \frac{Q}{\pi}\left[\ln\left\{\frac{\sqrt{(\xi-l)^2+\eta^2}\sqrt{(\xi-1/l)^2+\eta^2}}{\sqrt{\xi^2+\eta^2}}\right\} + i\left(\tan^{-1}\frac{\eta}{\xi-l} + \tan^{-1}\frac{\eta}{\xi-1/l} - \tan^{-1}\frac{\eta}{\xi}\right)\right] \\
&= V\xi\left(1+\frac{1}{\xi^2+\eta^2}\right) + \frac{Q}{\pi}\ln\left\{\frac{\sqrt{(\xi-l)^2+\eta^2}\sqrt{(\xi-1/l)^2+\eta^2}}{\sqrt{\xi^2+\eta^2}}\right\} \\
&\quad + i\left\{V\eta\left(1-\frac{1}{\xi^2+\eta^2}\right) + \frac{Q}{\pi}\left(\tan^{-1}\frac{\eta}{\xi-l} + \tan^{-1}\frac{\eta}{\xi-1/l} - \tan^{-1}\frac{\eta}{\xi}\right)\right\}. \quad \cdots (3.3.8)
\end{aligned}$$

Therefore, the streamline function Ψ is,

$$\begin{aligned}
\Psi &= V\eta\left(1-\frac{1}{\xi^2+\eta^2}\right) + \frac{Q}{\pi}\left(\tan^{-1}\frac{\eta}{\xi-l} + \tan^{-1}\frac{\eta}{\xi-1/l} - \tan^{-1}\frac{\eta}{\xi}\right) \\
&= Vr\sin\theta\left(1-\frac{1}{r^2}\right) + \frac{Q}{\pi}\left(\tan^{-1}\frac{r\sin\theta}{r\cos\theta-l} + \tan^{-1}\frac{r\sin\theta}{r\cos\theta-1/l} - \theta\right). \quad \cdots (3.3.9)
\end{aligned}$$

The streamline function for r equal to 1 is,

$$\Psi|_{r=1} = \frac{Q}{\pi}\left(\tan^{-1}\frac{r\sin\theta}{r\cos\theta-l} + \tan^{-1}\frac{r\sin\theta}{r\cos\theta-1/l} - \theta\right). \quad \cdots (3.3.10)$$

Let us consider in Fig. 3.3.2 a point C on the upper half of the circle with unit radius, O at (0, 0), A at ($1/l$, 0), and B at (l, 0). The relation,

$$\overline{\mathrm{OA}}:\overline{\mathrm{OC}} = \frac{1}{l}:l = 1:l = \overline{\mathrm{OC}}:\overline{\mathrm{OB}}, \quad \cdots (3.3.11)$$

leads to,

$$\varDelta\mathrm{ACO} \equiv \varDelta\mathrm{CBO}. \quad \cdots (3.3.12)$$

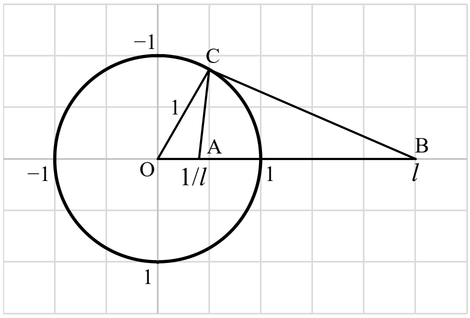

Fig. 3.3.2 Schematic diagram of the alternative *z*-pl. for the enhanced wake source model.

Therefore, for a point on the upper half of the circle,

$$\Psi|_{r=1,0\leq r<\pi} = \frac{Q}{\pi}\{(\pi - \angle\mathrm{CBO}) + (\theta + \angle\mathrm{CBO}) - \theta\} = Q. \qquad \cdots (3.3.13)$$

The discussion for the upper half circle AS_1B and its analogy for the lower one ensures that the circle with unit radius is a boundary as in Fig. 2.1.1. This also suggests that Eq. (2.1.9) also determines the coordinates of the separated streamline in the ζ_1-pl.

All the discussions in subsections 2.1.2 and 2.1.3, and those in subsection 2.2.1 except Eq. (2.2.12) holds for the ζ_1-pl. because they are independent of the complex potential. Therefore, Eq. (2.2.6) holds for the ζ_1-pl.

Since Eqs. (2.1.22), (2.2.10) and (2.2.11) hold, substituting Eq. (2.2.11) into Eq. (3.3.7) leads to, in the ζ_1-pl.,

$$Q = 2\pi MU(l^* - \cos\alpha)\cos\alpha, \qquad \cdots (3.3.14)$$

that replace Eq. (2.2.12).

The discussions in subsection 2.2.2 except Eqs. (2.2.21) through (2.2.25), and Eqs. (2.2.28) through (2.2.30) hold. Since Eq. (3.3.5) replaces Eq. (2.1.4), replacing $\cos\delta$ by l^* leads to equations corresponding to Eqs. (2.2.21) through (2.2.25) for the ζ_1-pl. Equations corresponding to Eqs. (2.2.24), (2.2.25) and (2.2.30) are,

$$\begin{aligned} C_{p(\theta)} &= 1 - \frac{(1+\cos^2\alpha - 2\cos\alpha\cos\theta)^2\sin^2\theta}{(\cos\theta - l^*)^2\{1 + {C_1}^2 + 9{C_3}^2 - 2C_1(1-3C_3)\cos 2\tilde{\theta}_{(\theta)} - 6C_3\cos 4\tilde{\theta}_{(\theta)}\}} \\ &= 1 - \frac{(1+\cos^2\alpha - 2\cos\alpha\cos\theta)^2\sin^2\theta}{(\cos\theta - l^*)^2\{(1 + C_1 - 3C_3)^2 - 4(C_1 - 12C_3 - 3C_1C_3)\cos^2\tilde{\theta}_{(\theta)} - 48C_3\cos^4\tilde{\theta}_{(\theta)}\}}, \\ &\qquad (\alpha \leq \theta \leq \pi \ or\ \Theta_s \leq \Theta \leq \pi), \quad \cdots (3.3.15) \end{aligned}$$

$$C_{pb} = 1 - \frac{\sin^6\alpha}{(\cos\alpha - l^*)^2\{1 + {C_1}^2 + 9{C_3}^2 - 2C_1(1-3C_3)\cos 4\alpha - 6C_3\cos 8\alpha\}}, \qquad \cdots (3.3.16)$$

and,

$$l^* = \cos\alpha + \frac{\sin^3\alpha}{\sqrt{(1 - C_{pb})\{1 + {C_1}^2 + 9{C_3}^2 - 2C_1(1-3C_3)\cos 4\alpha - 6C_3\cos 8\alpha\}}}, \qquad \cdots (3.3.17)$$

respectively.

Note that Eq. (2.2.31) calculating C_d uses Eq. (2.2.24) or Eq. (3.3.15) depending on whether l^* defined by Eq. (3.3.17) is greater or smaller than 1. Figure 3.3.3 explains how the variables in the z-pl. applied to the enhanced wake source model determine those in the ζ-pl. or ζ_1-pl.

The introduction of the alternative complex potential, Eq. (3.3.1), with the replacement of cosδ by l^*, removes the non-physical limitation, Eq. (3.1.8), and enhances the original d wake source model.

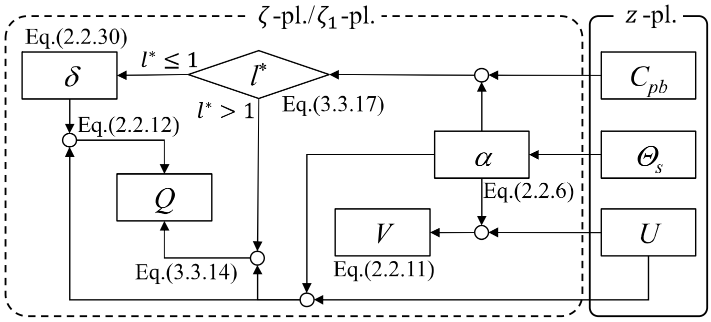

Fig. 3.3.3 Relation between variables in the z-pl., and those in the ζ- or ζ_1-pl. for the enhanced wake source model.

4. Case studies

This chapter presents the case studies in Ueno[15] of the enhanced wake source model applied to a container ship and a tanker with additional information and commentaries. The cases validate the enhancement explained in section 3.3 by showing separated streamlines, C_p distributions, and C_d dependencies on C_{pb} and Θ_s. The discussion includes comparisons of C_d distributions along ship length with Matsumoto's experimental data[11,12].

4.1 Subject ships and parameter setting

The subject ships are the containership and the tanker used in Matsumoto and Suemitsu[11] and Matsumoto[12]. They used segmented models that consist of ten parts of segments equally separated along ship length to measure hydrodynamic lateral forces acting on each segment. Figure 4.1.1 shows the arrangement of the segmented model[11,12].

Table 4.1.1 lists the principal particulars of the subject segmented ship models. Each ship's model length is 3.0 m. Figures 4.1.2 and 4.1.3 show the body plans approximated by Lewis form[14]. The original lines, ship hull form data, and Lewis form parameters are not presented here. Values in Figs. 4.1.2 and 4.1.3 stand for longitudinal coordinates of cross-sections, X, divided by ship length, L_{pp}. The origin of X is at midship pointing fore. These coordinates correspond to those of Matsumoto's tank test data[11,12]. The aft-end cross-section of containership where X/L_{pp} is equal to -0.45 is not applied to the enhanced wake source model calculation because its shape is out of the range of Lewis form approximation. The Tanker's parallel part of which X/L_{pp} is from -0.10 to 0.25 has an identical shape of cross-section.

Their tank test data include those measured when the ship models were towed laterally. The data, therefore, clarified the longitudinal C_d distribution corresponding to Eq. (2.2.31).

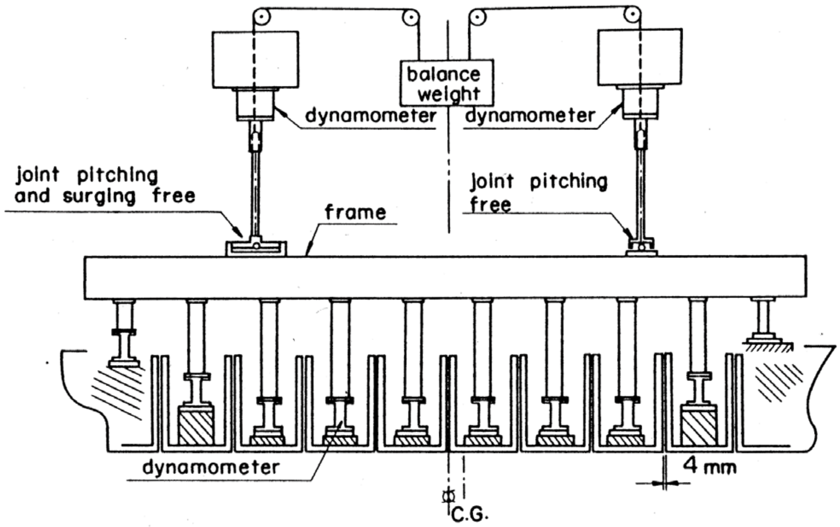

Fig. 4.1.1 Arrangement of the segmented model. Reprinted from Matsumoto and Suemitsu[11] with permission from The Japan Society of Naval Architects and Ocean Engineers.

Table 4.1.1 Principal particulars of subject ships in model scale

	Containership	Tanker	Note
Load.	Trial	Full	Loading condition
L_{pp} (m)	3.0000	3.0000	Length between perpendiculars
B_r (m)	0.4354	0.5236	Breadth
d_m (m)	0.1457	0.1956	Drought at midship
τ (m)	0.0172	0.0000	Trim by stern
l_{cb} (%)	1.8100	-2.4800	Center of buoyancy, midship-to-aft ship length ratio
Vol. (m^3)	0.1069	0.2534	Displaced volume
S_w (m^2)	1.5019	2.3987	Wetted surface area
C_b	0.5617	0.8250	Block coefficient
Scale	1/58.3	1/104.7	Ratio to full-scale ship

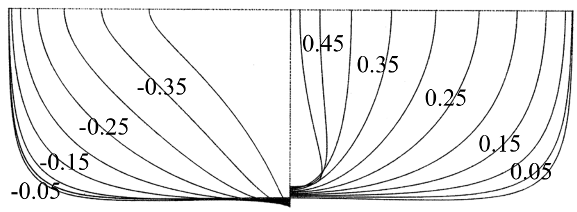

Fig. 4.1.2 Containership body plan approximated by Lewis form.

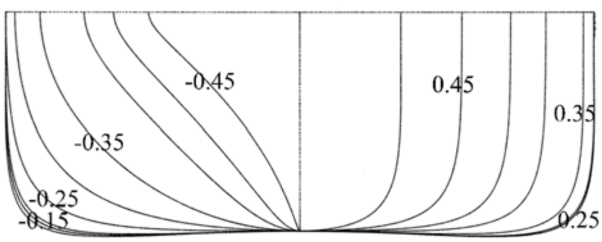

Fig. 4.1.3 Tanker body plan approximated by Lewis form.

The input parameters to the enhanced wake source model are U, C_{pb}, and Θ_s. The lateral towing velocities U of the containership model in the tank test were 0.271, 0.542, and 0.813 m/s[11,12]. In this case study, the flow velocity U is 0.271 m/s for the containership model. The reason to select the lowest velocity is that the data should be mostly free from wave-making effects among those in three kinds of velocities. The flow velocity for the tanker model is 0.651 m/s as in the tank test[11,12]. The other parameters C_{pb} and Θ_s are set as follows because their theoretical estimation is difficult and out of the scope of this study. Firstly, assume appropriate Θ_s around the bilge corner or keel of each cross-section. Secondly, set C_{pb} to make the calculated C_d at the closest cross-sections to midship nearly equal to the corresponding tank test data. Lastly, assume the C_{pb} of other cross-sections is equal to that at the closest cross-sections to midship. Note that larger Θ_s means the upstream region, while smaller Θ_s means the downstream region.

The second through fourth columns from left in Tables 4.1.2 and 4.1.3 list the input parameters U, Θ_s, and C_{pb} for the containership and tanker, respectively.

Because U of the containership is low and cross-sections have relatively round shapes at the bilge corner or center keel, the values of Θ_s are assumed equal to or smaller than 90° except at X/L_{pp} is equal to 0.45 and 0.35. Θ_s at X/L_{pp} equal to 0.45 is assumed larger than 90° due to its slender shape. Θ_s at X/L_{pp} equal to 0.35 is assumed slightly larger than 90° due to the continuity of the successive aft cross-section. Comparison of calculated C_d at the closest cross-sections to midship with Matsumoto's tank test data assumed C_{pb} equal to -0.464 for the containership.

The inflow velocity U for the tanker is larger than that of the containership and the most of tanker's cross-sections have bilge corners with relatively small radii of curvature. These are the reasons why Θ_s is assumed around upstream bilge corners, or points of Θ_s equal to or larger than 90°. The tank test data around midship cross-sections for the tanker leads to the assumed C_{pb} value equal to -0.950, lower than that of the containership probably due to larger U. Note that a trial calculation in which Θ_s were assumed at around downstream bilge corners led to C_{pb} equal to -1.488 and those cross-sections at X/L_{pp} equal to -0.25 and -0.35 did not satisfy Eq. (2.2.42), the physical requirement of the separated streamline.

Table 4.1.2 Flow parameters for the enhanced wake source model (Containership)

X/L_{pp}	U (m/s)	C_{pb}	Θ_s (deg)	Q/U	C_d	α(deg)	δ(deg)	l^*	Q/V
0.45	0.271	-0.464	100	0.2577	1.0447	58.50	—	1.4042	5.5451
0.35	do.	do.	95	0.2275	0.7609	49.84	—	1.1709	3.2940
0.25	do.	do.	90	0.1852	0.5409	45.00	1.92	—	1.8368
0.15	do.	do.	60	0.1220	0.4251	34.78	17.56	—	0.8296
0.05	do.	do.	36	0.0760	0.4384	22.73	9.01	—	0.4104
-0.05	do.	do.	35	0.0738	0.4629	21.37	7.04	—	0.3847
-0.15	do.	do.	40	0.0809	0.4149	25.36	12.35	—	0.4601
-0.25	do.	do.	90	0.2041	0.5388	45.00	12.04	—	1.7022
-0.35	0.271	-0.464	90	0.2943	0.7406	45.00	—	1.2096	3.1666
-0.45	—	—	—	—	—	—	—	—	—

X/L_{pp} : Long. coord. of cross-section, ratio to ship length (pointing fore from midship)

Table 4.1.3 Flow parameters for the enhanced wake source model (Tanker)

X/L_{pp}	U (m/s)	C_{pb}	Θ_s (deg)	Q/U	C_d	α(deg)	δ(deg)	l^*	Q/V
0.45	0.651	-0.950	121	0.3639	1.2782	62.14	—	1.1280	4.1563
0.35	do.	do.	141	0.5528	1.4063	67.85	—	1.2881	5.7172
0.25	do.	do.	142	0.5958	1.4567	68.21	—	1.3352	6.0646
0.15	do.	do.	do.	do.	do.	do.	—	do.	do.
0.05	do.	do.	do.	do.	do.	do.	—	do.	do.
-0.05	do.	do.	142	0.5958	1.4567	68.21	—	1.3352	6.0646
-0.15	do.	do.	142	0.5764	1.4285	68.12	—	1.3076	5.8817
-0.25	do.	do.	140	0.4658	1.2552	66.07	—	1.1280	4.5424
-0.35	do.	do.	97	0.2478	1.0076	48.07	18.66	—	1.7543
-0.45	0.651	-0.950	90	1.2873	1.7883	45.00	—	2.8457	13.4343

X/L_{pp} : Long. coord. of cross-section, ratio to ship length (pointing fore from midship)

4.2 Separated streamline and C_p distribution

Figures 4.2.1 through 4.2.9 and Figs. 4.2.10 through 4.2.16 are the calculation results of the containership and the tanker, respectively. Each figure consists of three subfigures. The top subfigure is a ζ-pl. showing a separation point by the open circle, separated streamline, and positions of the double sources of strength $2Q$ except at the origin by the filled circle. Whether the filled circles are on the circular cylinder or the ξ-axis distinguishes which wake source model is used for calculation, the original or the enhanced one. Note that one of the two double source positions for the tanker's cross-section at X/L_{pp} equal to -0.45 is not within the display. The middle subfigure is a z-pl. showing a separated streamline in a physical plane. The bottom subfigure is also a z-pl. showing C_p distribution on a ship cross-section. The line connecting consecutive edges of assumed vectors representing C_p normal to and originating from the surface of a cross-section stands for the pressure distribution. The scale is as C_p equal to 1 corresponds to the vector magnitude equal to $B_r/4$ in each cross-section.

The right-hand six columns in Tables 4.1.2 and 4.1.3 list calculated values. Results of cross-sections having δ values are by the original wake source model, while those having l^* values are by the enhanced wake source model. The magnitude of C_d correlates well with that of Q/U and that of Q/V representing the depth of separated streamline in the z-pl. and the ζ-pl., respectively, as mentioned in subsection 2.2.1.

The enhanced wake source model calculates the two fore and one aft-end cross-section of the containership, and all but one cross-section of the tanker. Most of the separated streamline and C_p distribution in the z-pls. seem appropriate. Negative C_p seems to appear in the high flow velocity region, especially around bilge corners and center keels. However, the separated streamline of the tanker's aft-end cross-section where X/L_{pp} is equal to -0.45 seems to be unnatural. The acute center keel should result in large values of C_d, Q/U, and Q/V. The Lewis form approximation is quite poor around the center keel of this aft-end cross-section, though the comparison with the original sectional shape is not shown here.

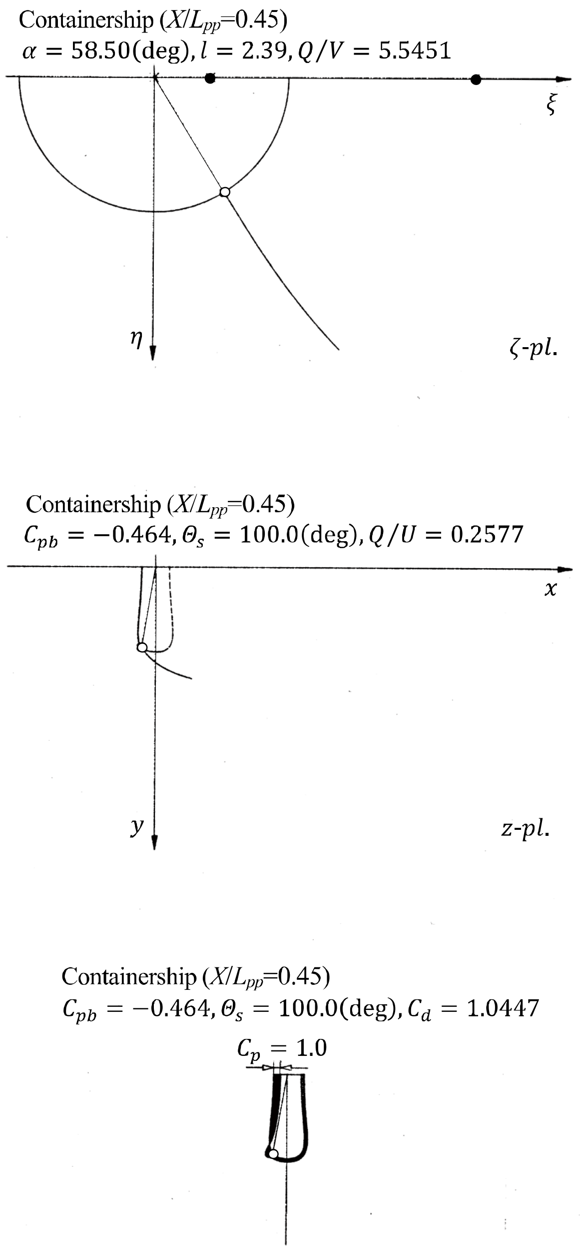

Fig. 4.2.1 Containership's sectional flow and C_p at X/L_{pp}=0.45.

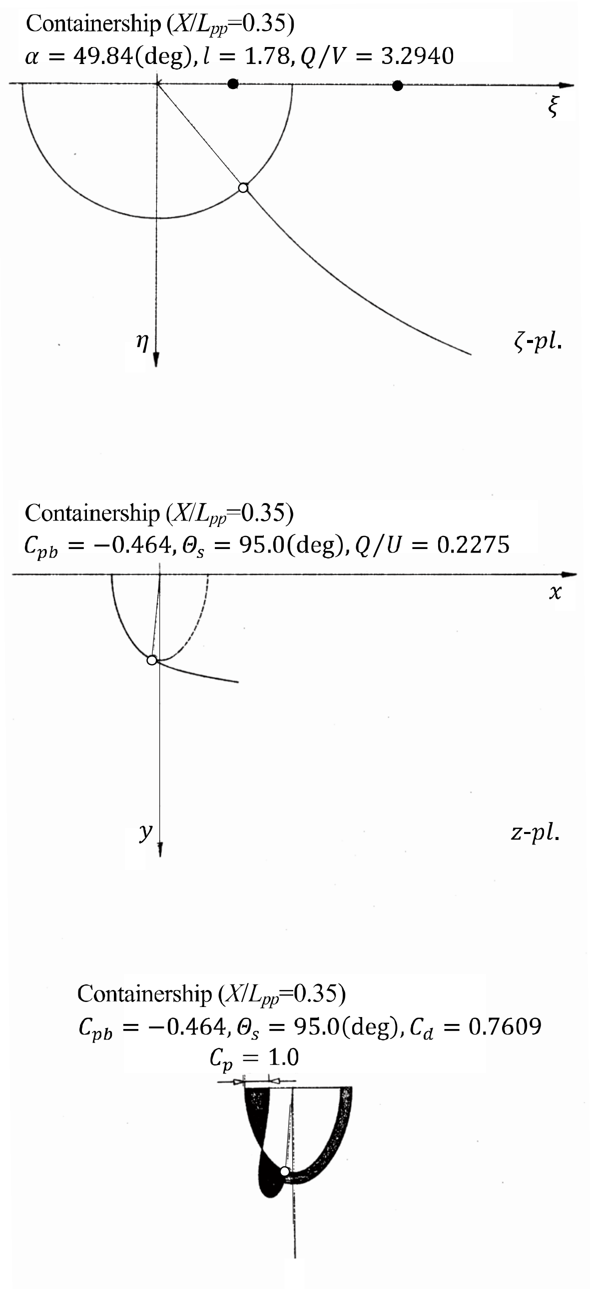

Fig. 4.2.2 Containership's sectional flow and C_p at X/L_{pp}=0.35.

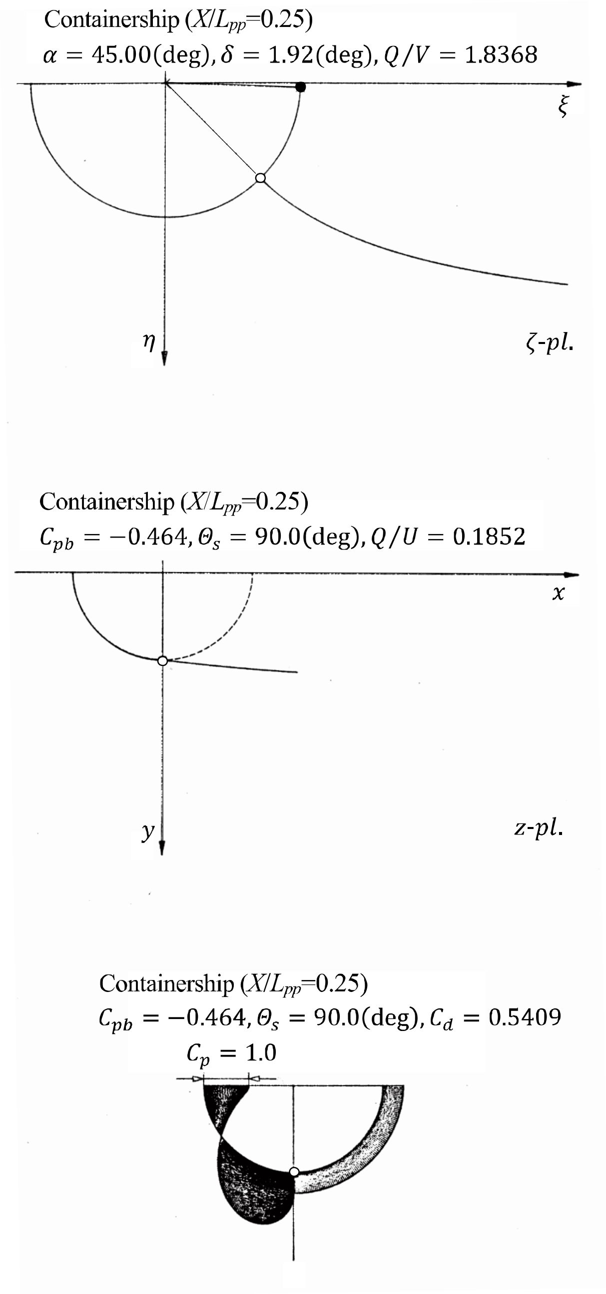

Fig. 4.2.3 Containership's sectional flow and C_p at X/L_{pp}=0.25.

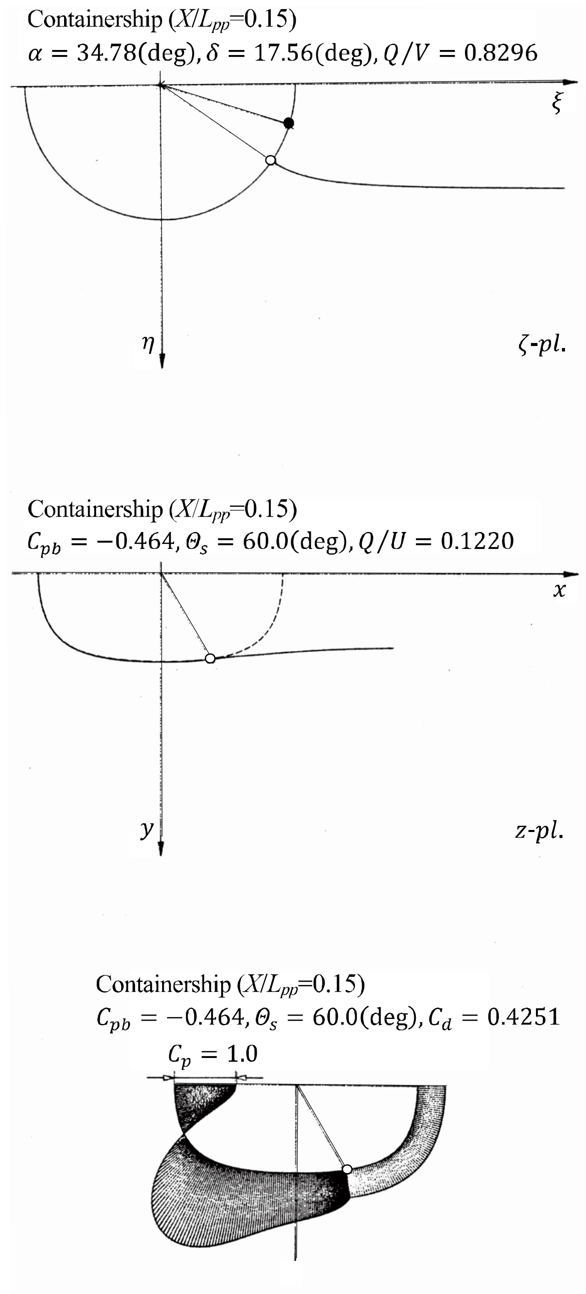

Fig. 4.2.4 Containership's sectional flow and C_p at X/L_{pp}=0.15.

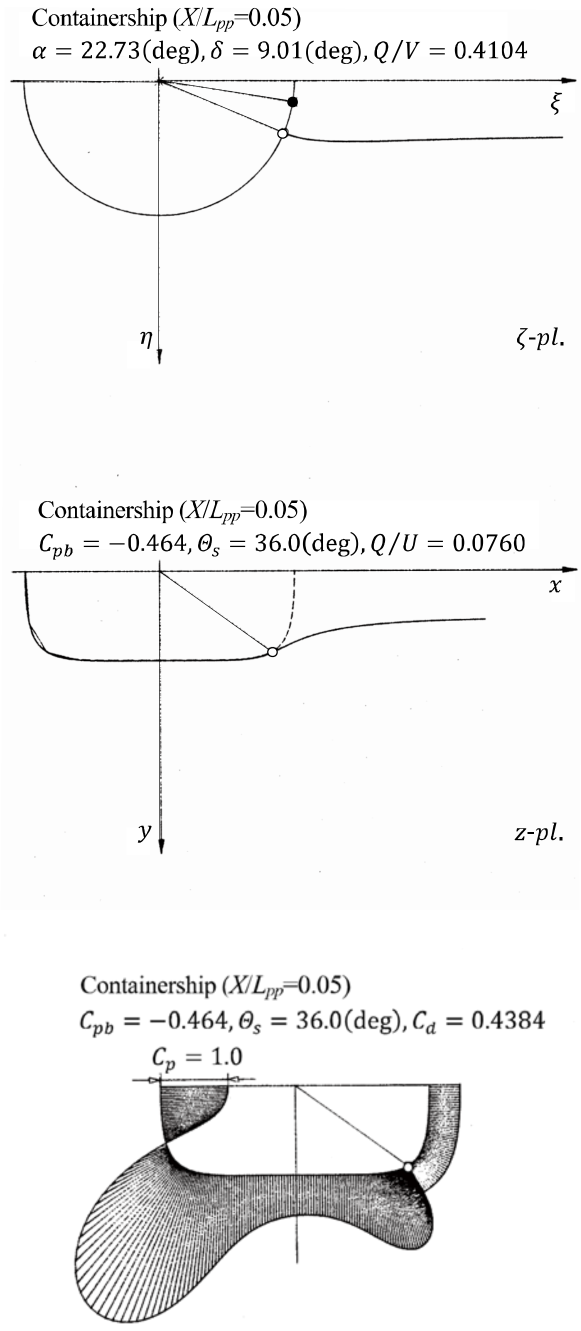

Fig. 4.2.5 Containership's sectional flow and C_p at X/L_{pp}=0.05.

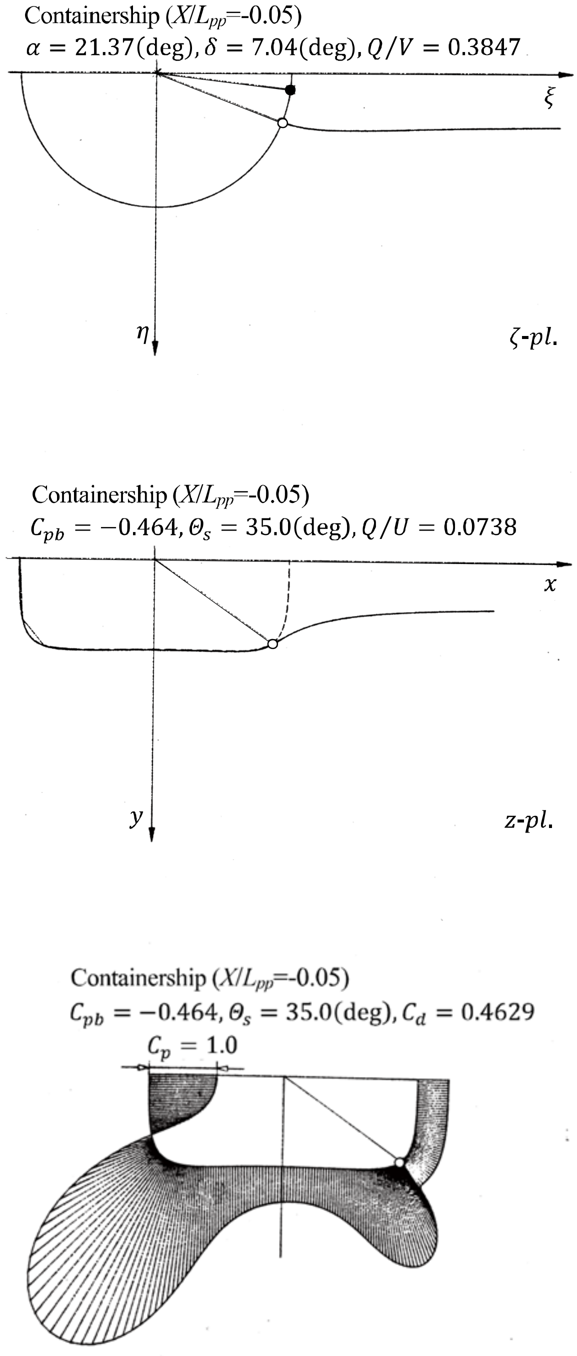

Fig. 4.2.6 Containership's sectional flow and C_p at X/L_{pp}=-0.05.

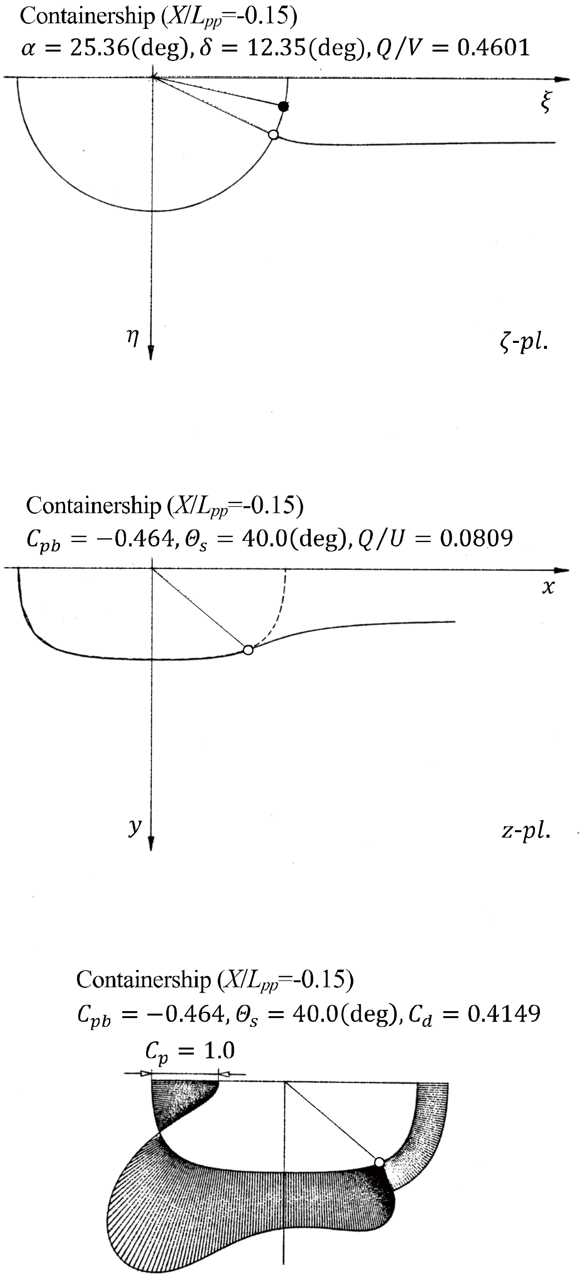

Fig. 4.2.7 Containership's sectional flow and C_p at X/L_{pp}=-0.15.

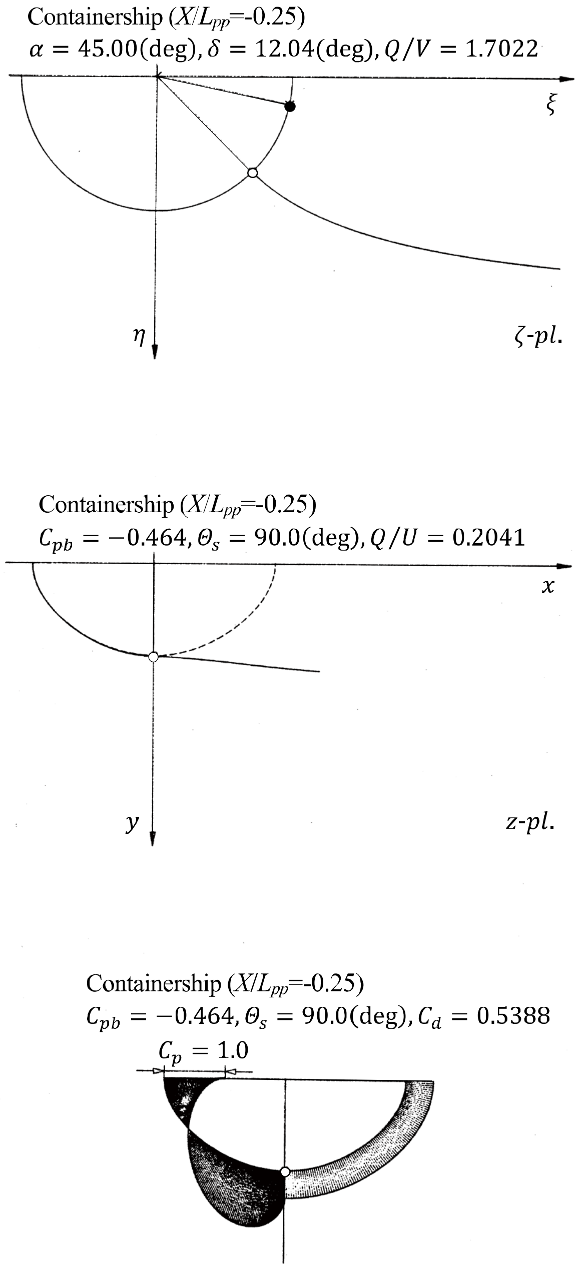

Fig. 4.2.8 Containership's sectional flow and C_p at X/L_{pp}=-0.25.

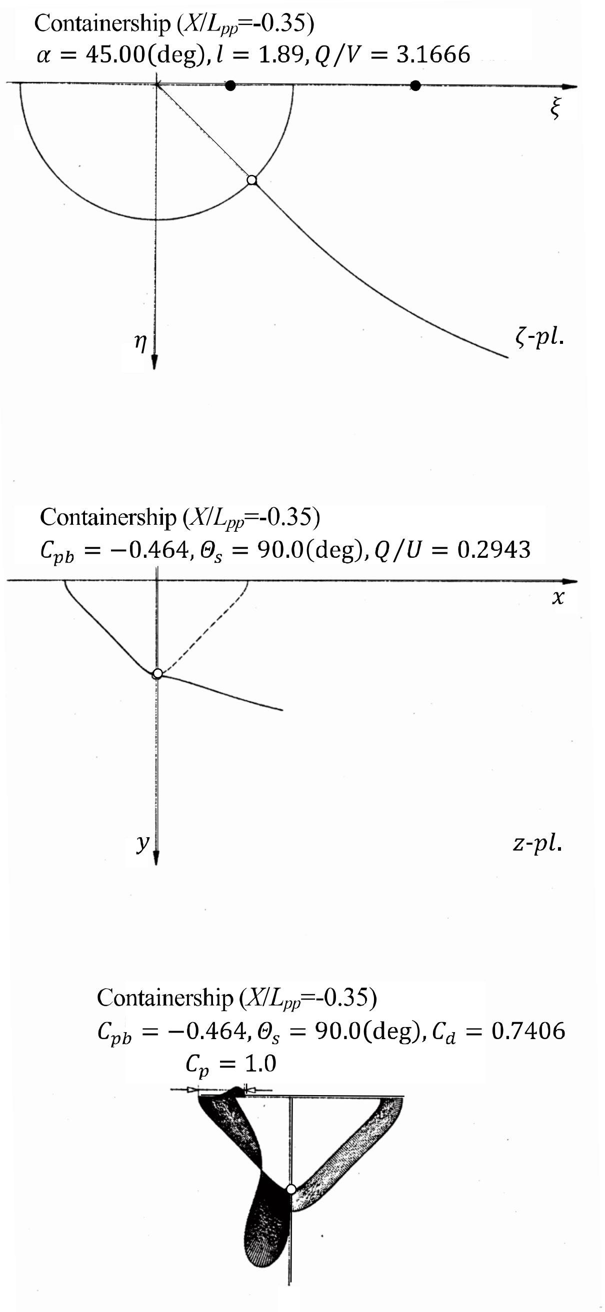

Fig. 4.2.9 Containership's sectional flow and C_p at X/L_{pp}=-0.35.

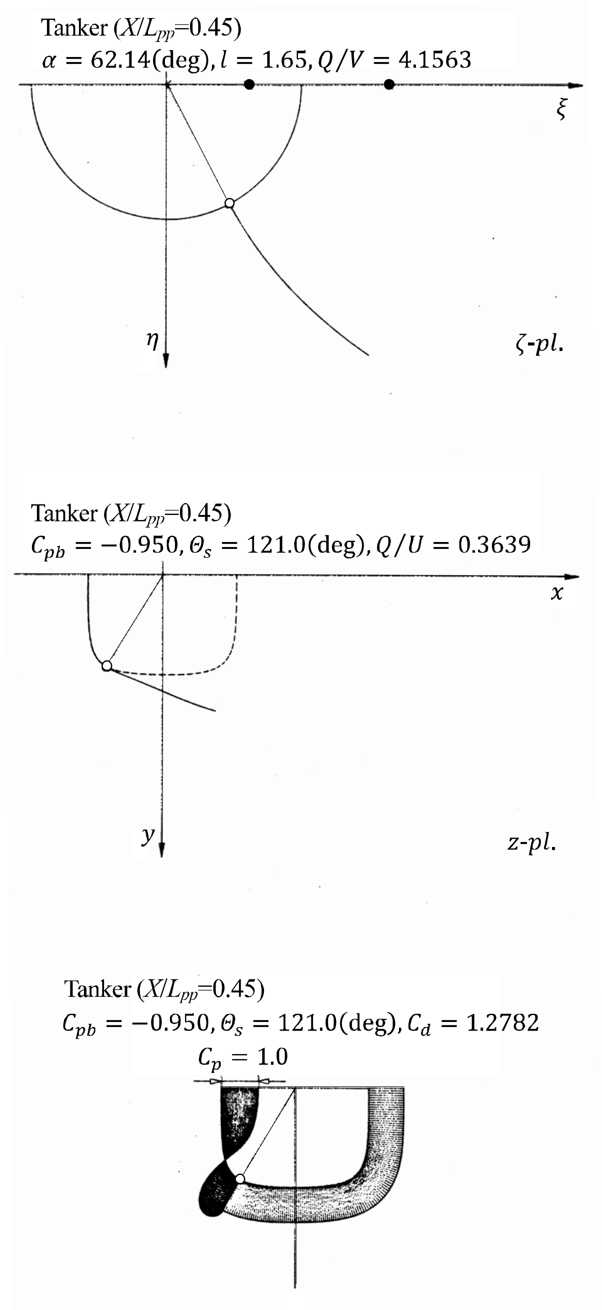

Fig. 4.2.10 Tanker's sectional flow and C_p at X/L_{pp}=0.45.

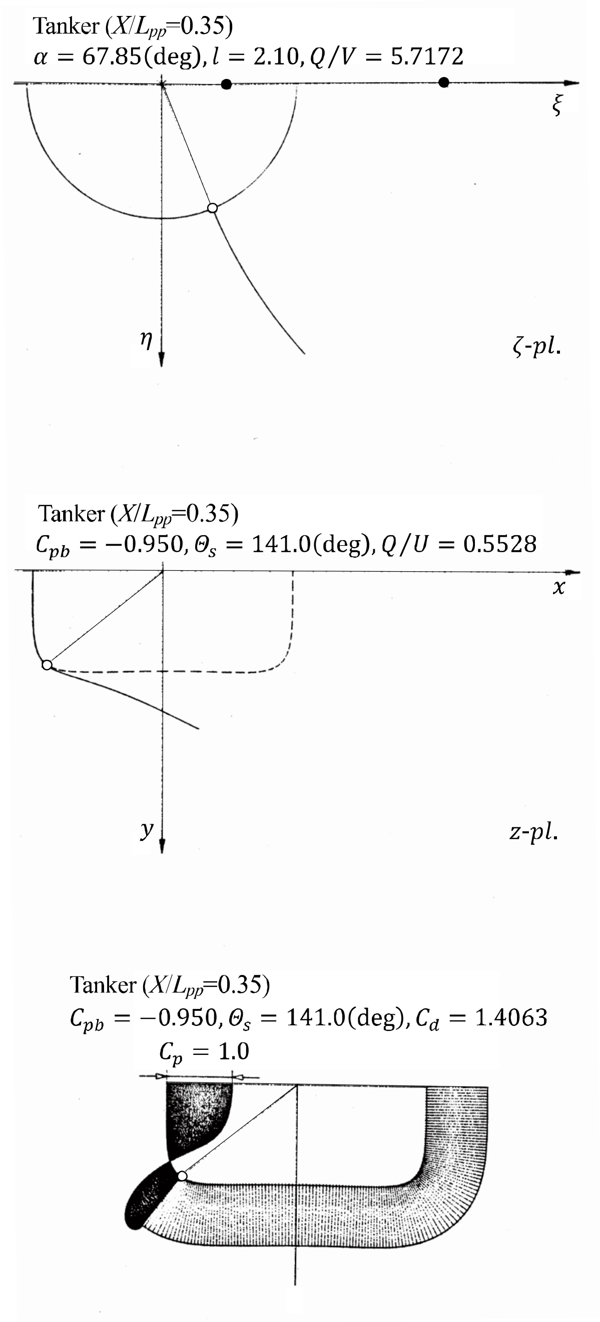

Fig. 4.2.11 Tanker's sectional flow and C_p at X/L_{pp}=0.35.

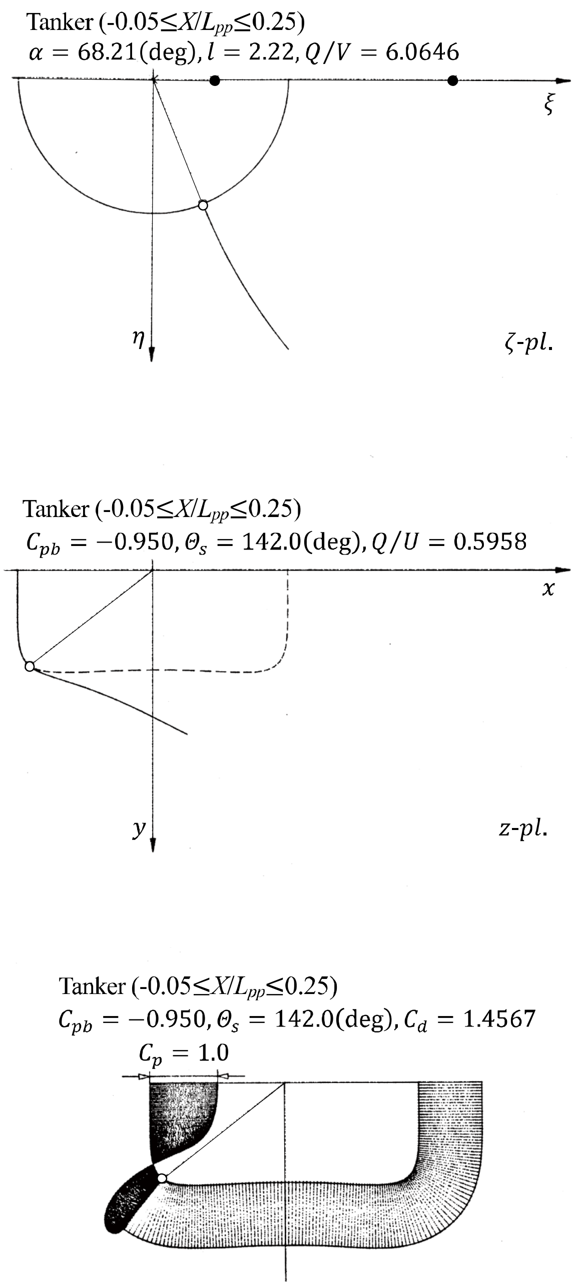

Fig. 4.2.12 Tanker's sectional flow and C_p at -0.05≤X/L_{pp}≤0.25.

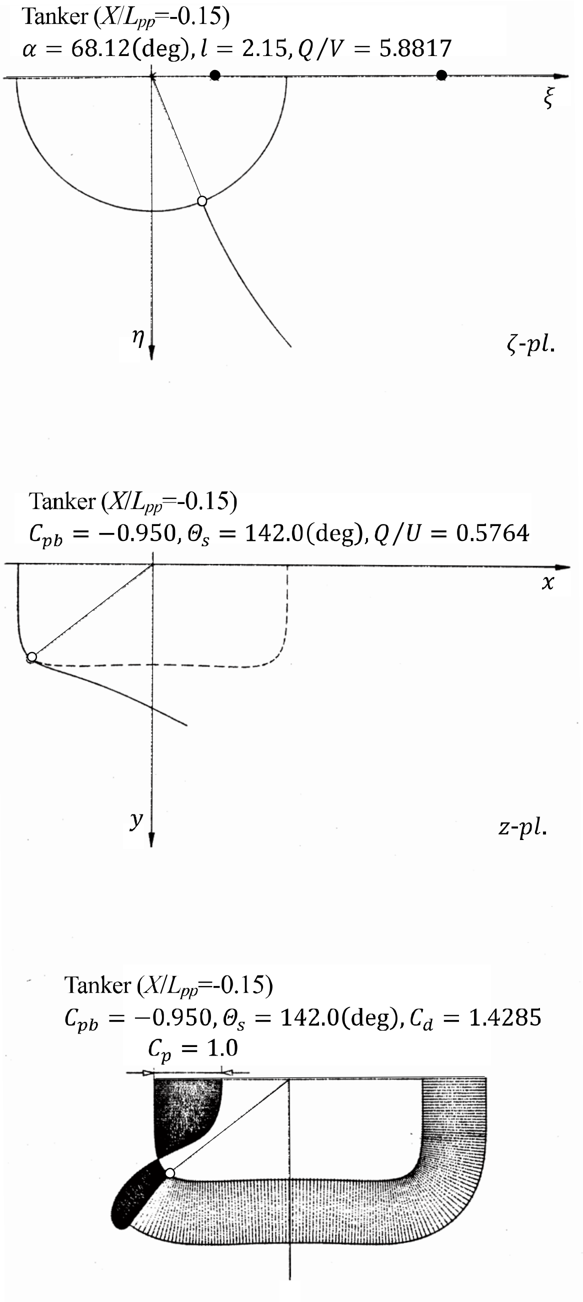

Fig. 4.2.13 Tanker's sectional flow and C_p at X/L_{pp}=-0.15.

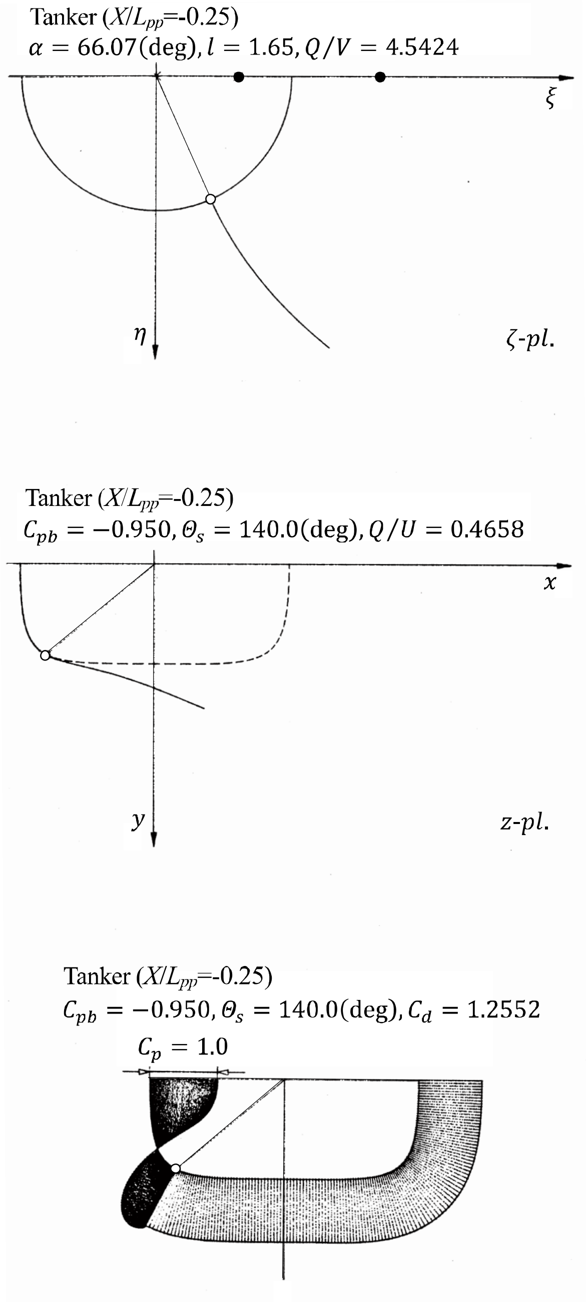

Fig. 4.2.14 Tanker's sectional flow and C_p at X/L_{pp}=-0.25.

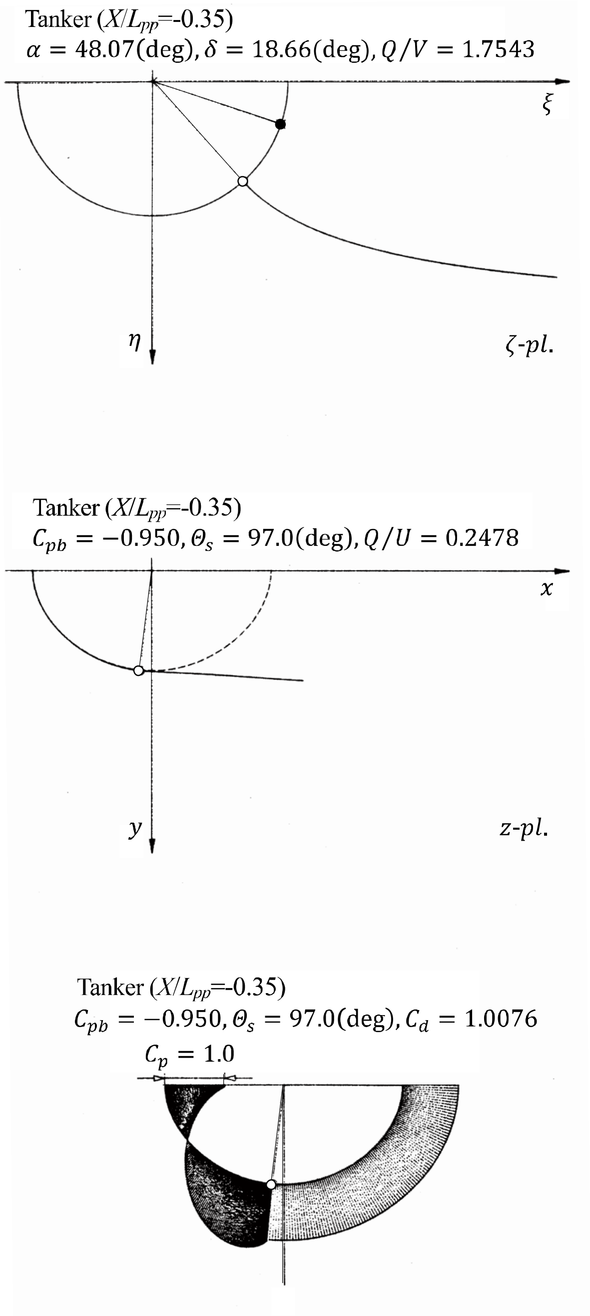

Fig. 4.2.15 Tanker's sectional flow and C_p at X/L_{pp}=-0.35.

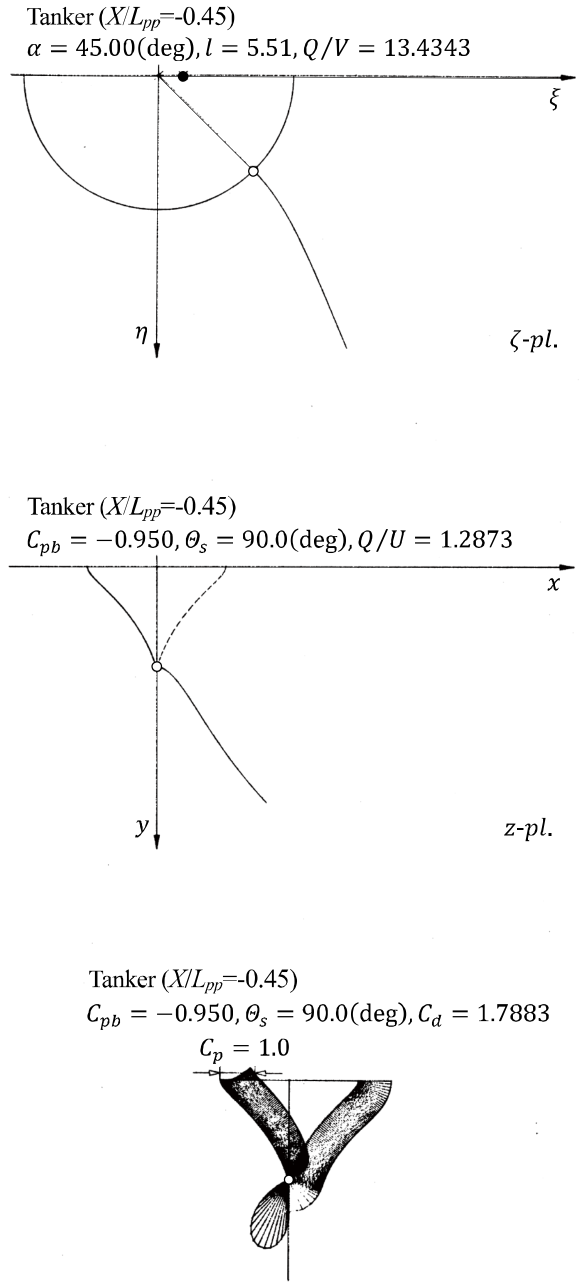

Fig. 4.2.16 Tanker's sectional flow and C_p at X/L_{pp}=-0.45.

4.3 C_d dependency on Θ_s and C_{pb}

To have a wider perspective than specific cases presented in the previous section 4.2, this section clarifies C_d dependency on Θ_s and C_{pb}. Figures 4.3.1 through 4.3.9 for the containership and Figs. 4.3.10 through 4.3.16 for the tanker show C_d contours as a function of Θ_s and C_{pb}. The flow speed U is 0.271 m/s for the containership and 0.651 m/s for the tanker as shown in Tables 4.1.2 and 4.1.3, respectively. A filled circle in each figure stands for the calculation results shown in Tables 4.1.2 and 4.1.3, and Figs. 4.2.1 through 4.2.16. All figures also show lines of g_1 and g_2 in Eq. (3.2.2). Note that part of the contours near the upper and right-hand edges of each figure seems distorted due to unknown plotting algorism effects and, therefore, must be ignored. Also, note that the contour for the tanker's cross-section at X/L_{pp} equal to -0.45 is not displayed because the C_d variation range exceeds 100 due to the acute center keel.

As explained in subsection 2.2.3, calculation results in the hatched region below the g_1-line has separated streamlines intersecting the surface of ship cross-sections, which is physically irrational. The enhanced wake source model is limited only by the g_1-line as the lowest C_{pb}, while the original wake source model is additionally limited by the g_2 line as the highest C_{pb} as in Eq. (3.1.2).

It is reasonable that C_d decreases as C_{pb} increases for a constant Θ_s. It is also reasonable that the smaller radius of curvature is the larger C_d is. On the other hand, the rough trend for a constant C_{pb} is that C_d increases as Θ_s increases. However, the local maximum tends to appear around the upstream bilge corner, and the local minim is around the downstream bilge corner, though no such clear trend appears for cross-sections without bilge corners.

Characteristics of g_1 reflects well the cross-section shape. g_1 has a small value around the bilge corner or center keel where the radius of curvature is small. Since g_2 becomes smaller in the upstream bilge corner than in the downstream one, most of the flow fields in which separations occur at the upstream bilge corner must rely on the enhanced wake source model. In general, the larger Θ_s is assumed, the more often the enhanced wake source model is employed. These facts confirm that the enhanced wake source model is more effective than the original one for applying to ship cross-sections.

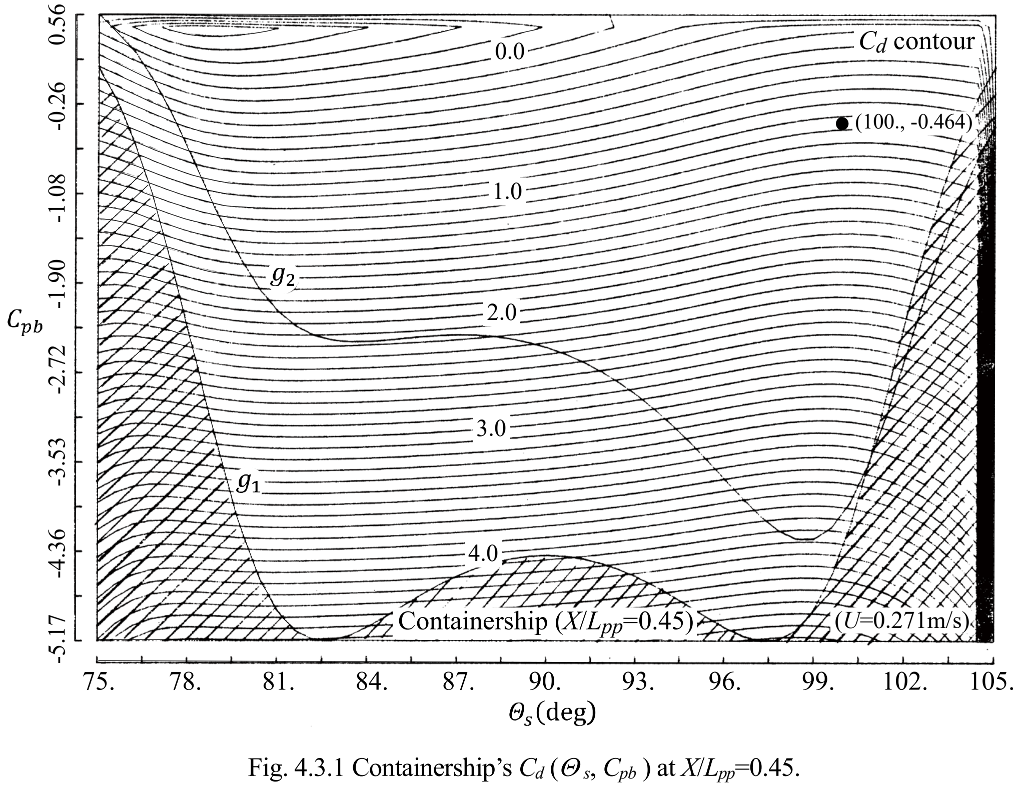

Fig. 4.3.1 Containership's C_d (Θ_s, C_{pb}) at X/L_{pp}=0.45.

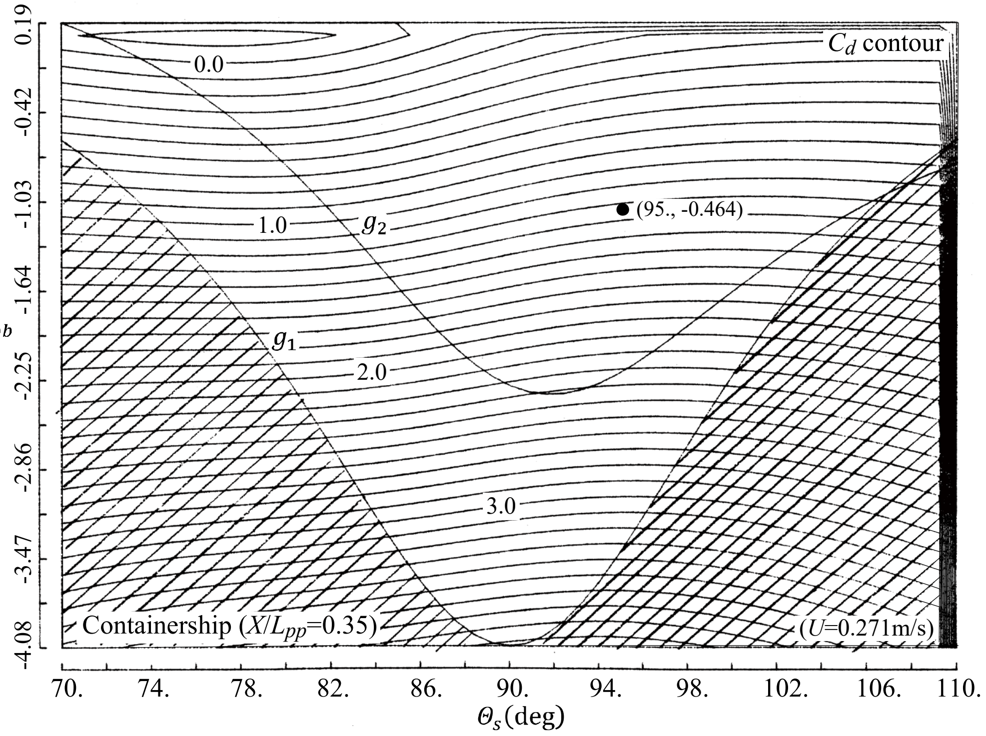

Fig. 4.3.2 Containership's C_d (Θ_s, C_{pb}) at X/L_{pp}=0.35.

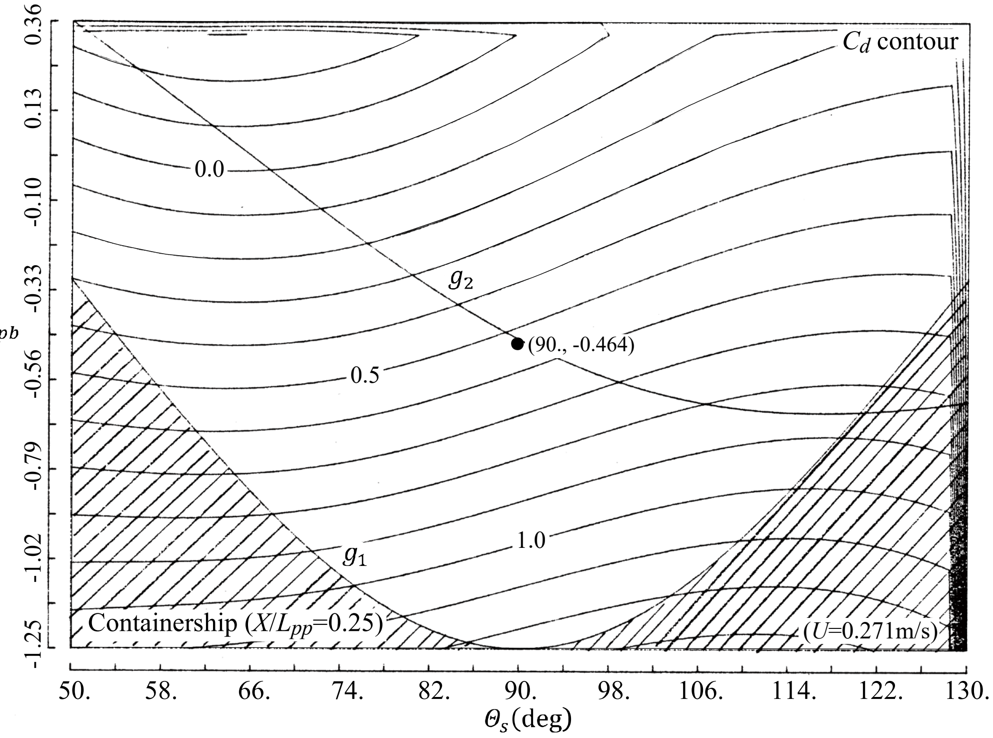

Fig. 4.3.3 Containership's C_d (Θ_s, C_{pb}) at X/L_{pp}=0.25.

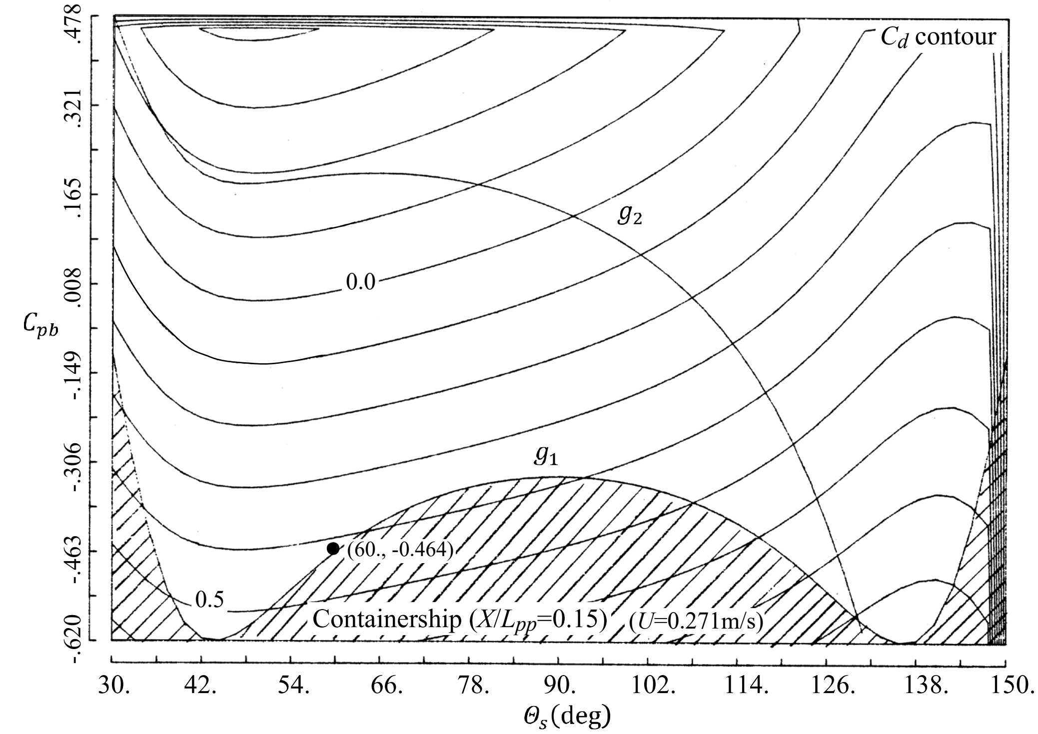

Fig. 4.3.4 Containership's C_d (Θ_s, C_{pb}) at X/L_{pp}=0.15.

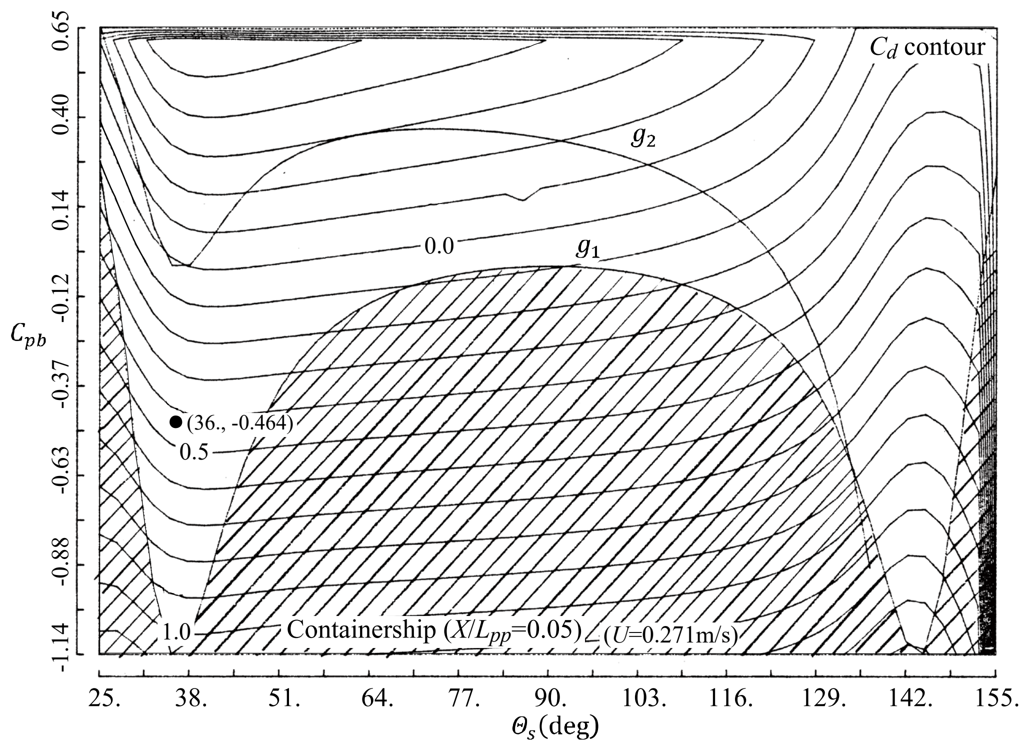

Fig. 4.3.5 Containership's C_d (Θ_s, C_{pb}) at X/L_{pp}=0.05.

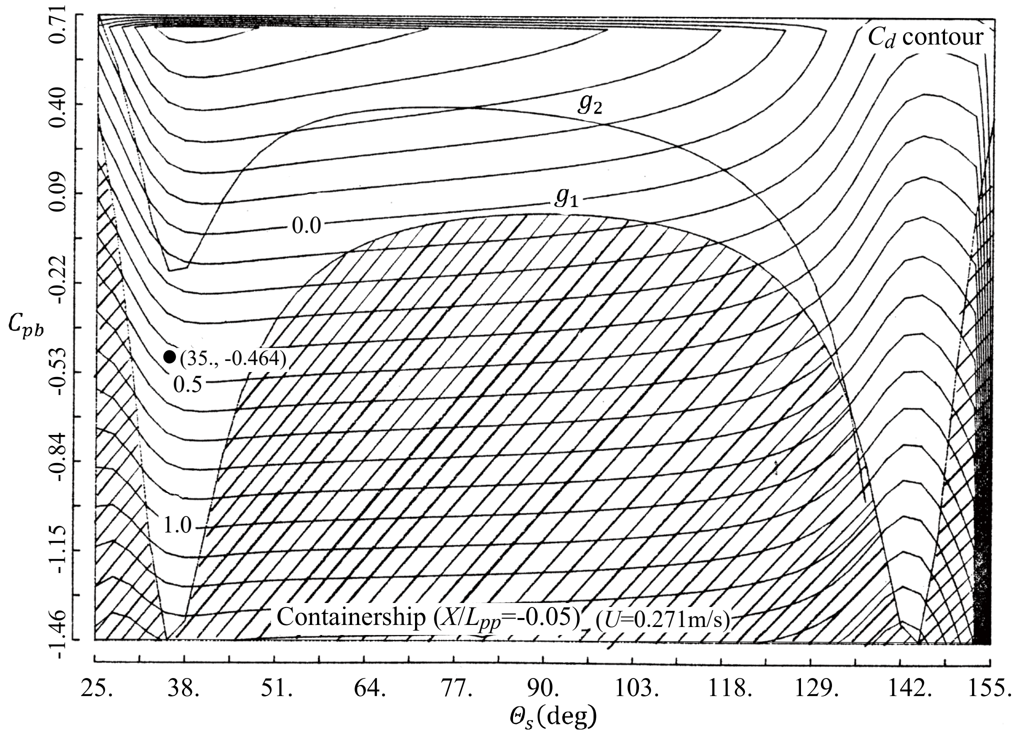

Fig. 4.3.6 Containership's C_d (Θ_s, C_{pb}) at X/L_{pp}=-0.05.

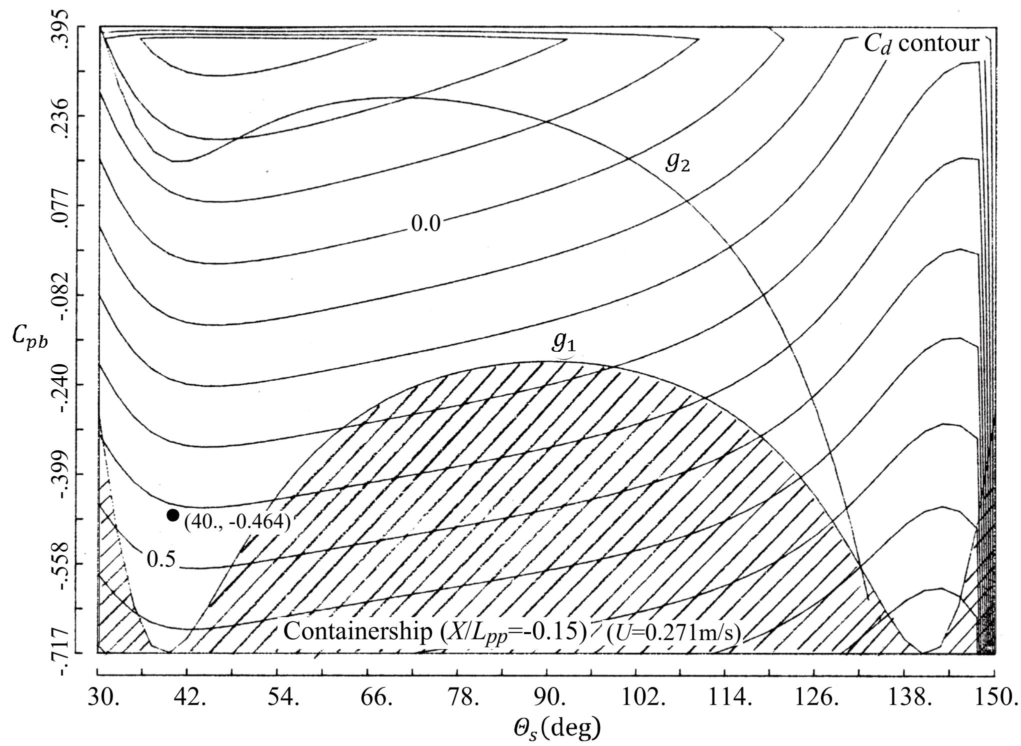

Fig. 4.3.7 Containership's C_d (Θ_s, C_{pb}) at X/L_{pp}=-0.15.

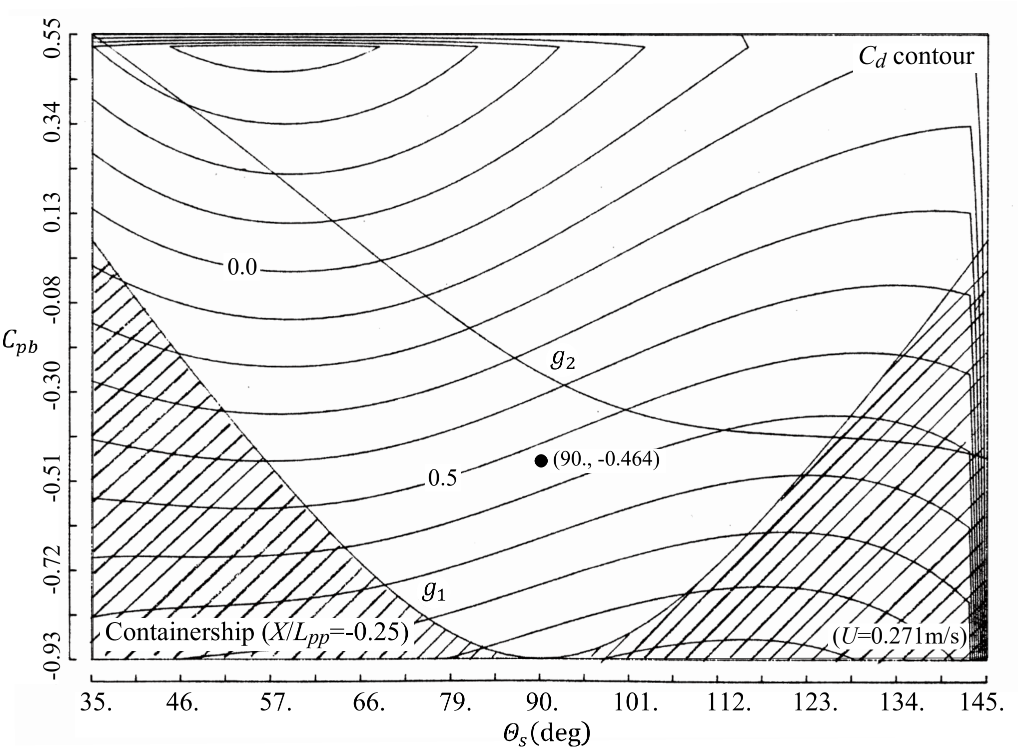

Fig. 4.3.8 Containership's C_d (Θ_s, C_{pb}) at X/L_{pp}=-0.25.

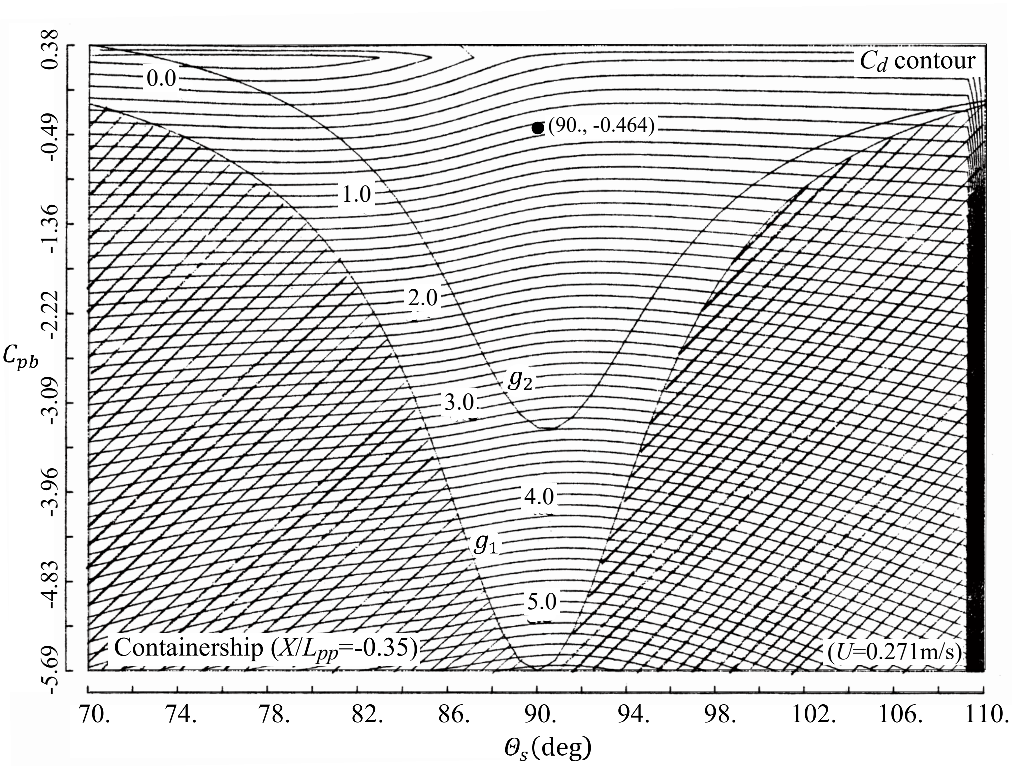

Fig. 4.3.9 Containership's C_d (Θ_s, C_{pb}) at X/L_{pp}=-0.35.

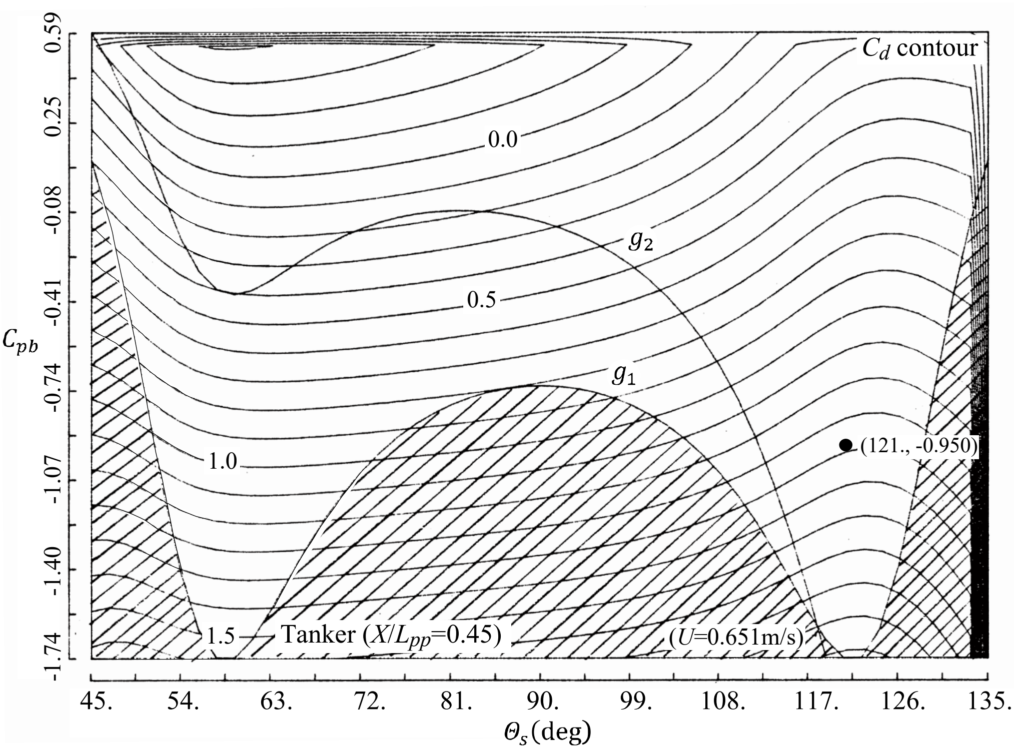

Fig. 4.3.10 Tanker's C_d (Θ_s, C_{pb}) at X/L_{pp}=0.45.

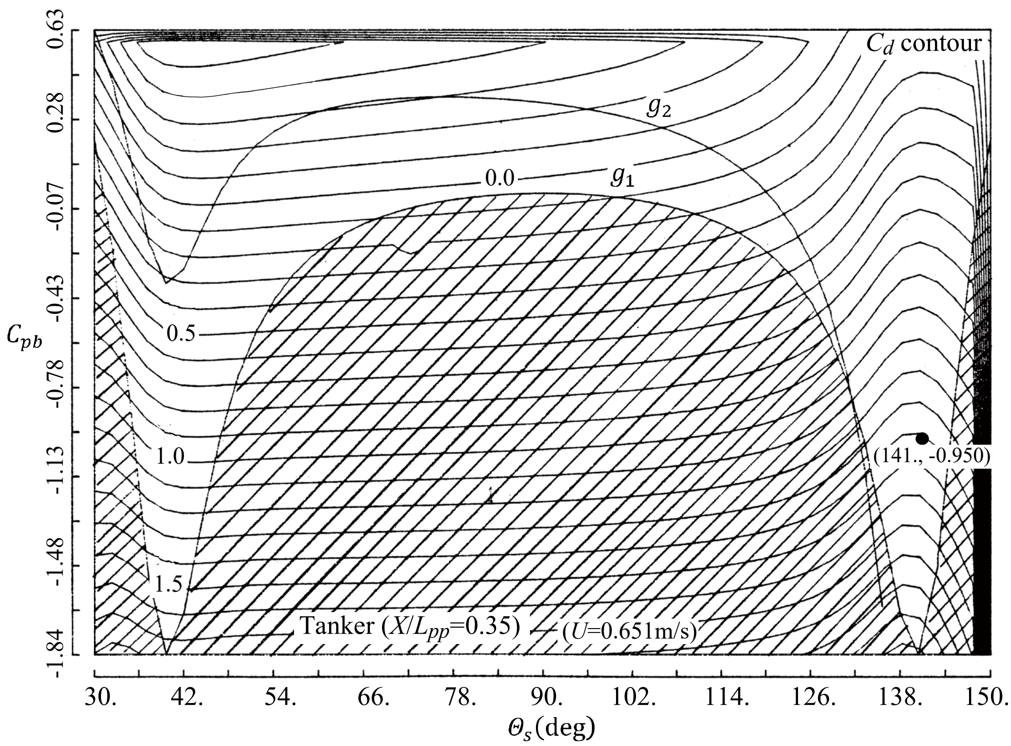

Fig. 4.3.11 Tanker's C_d (Θ_s, C_{pb}) at X/L_{pp}=0.35.

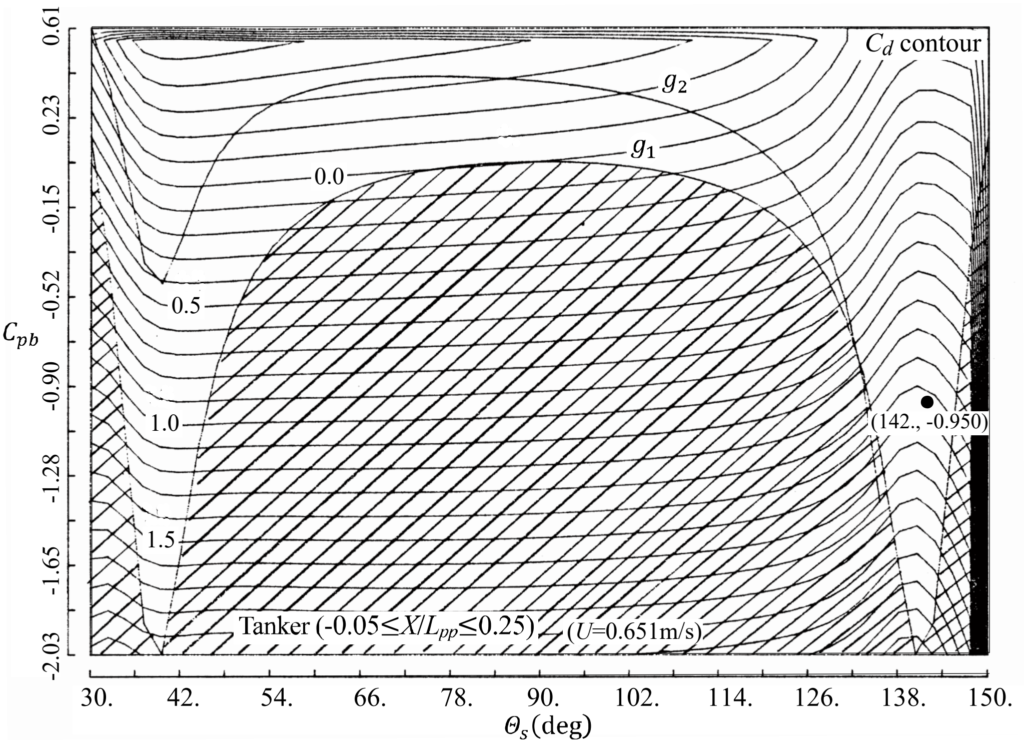

Fig. 4.3.12 Tanker's C_d (Θ_s, C_{pb}) at -0.05≤X/L_{pp}≤0.25.

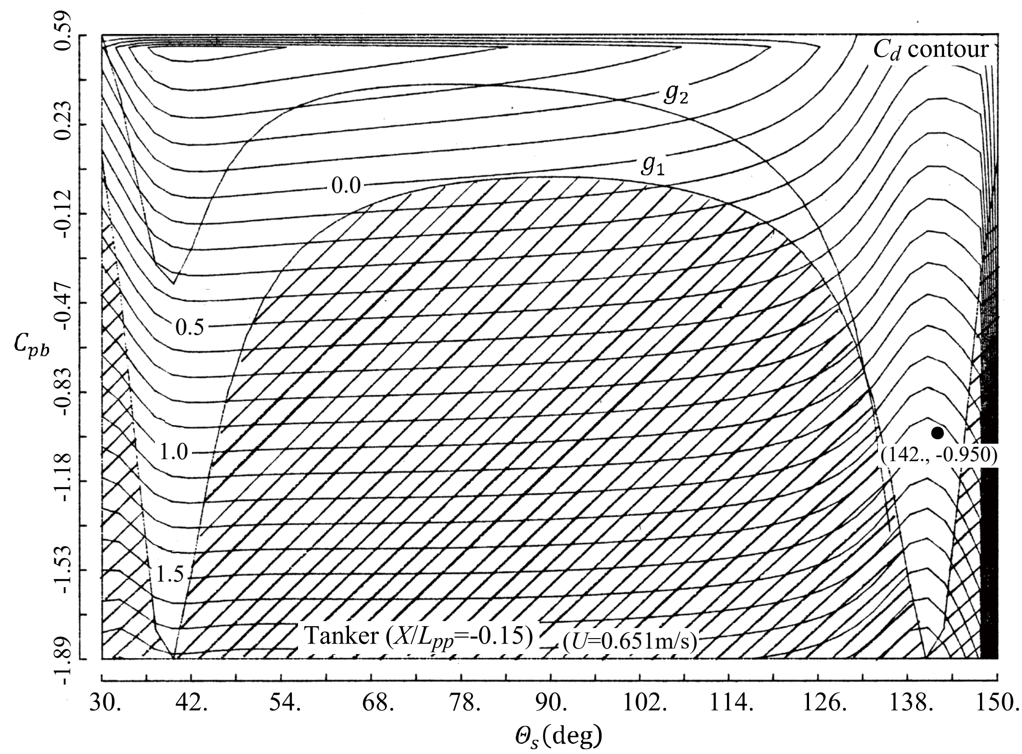

Fig. 4.3.13 Tanker's C_d (Θ_s, C_{pb}) at X/L_{pp}=-0.15.

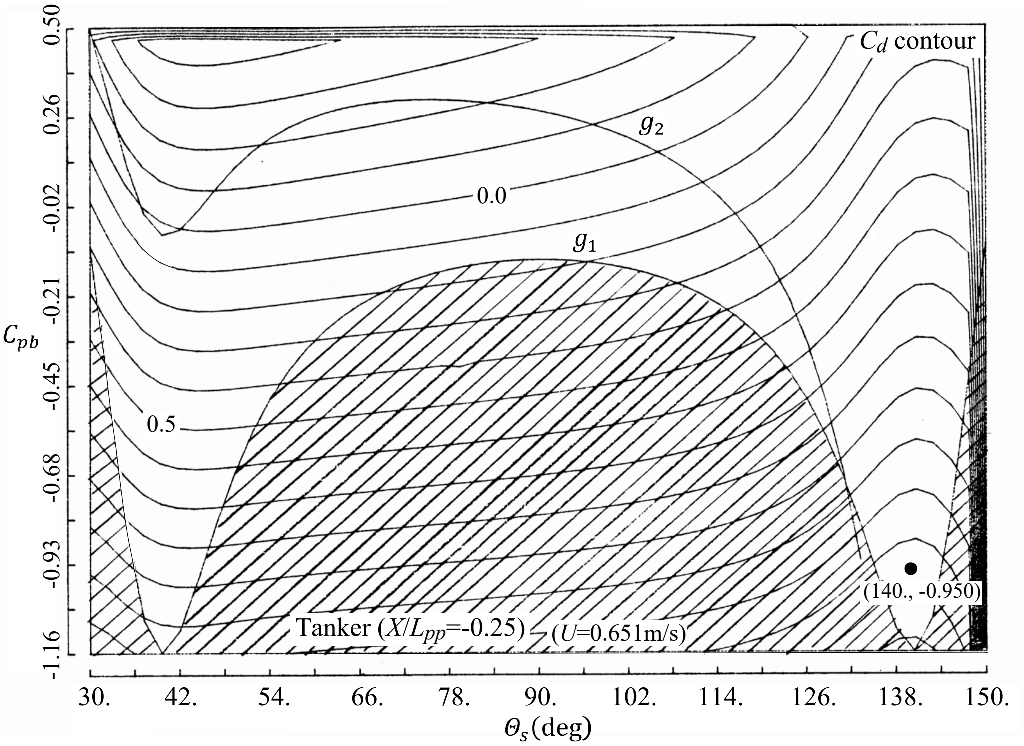

Fig. 4.3.14 Tanker's C_d (Θ_s, C_{pb}) at X/L_{pp}=-0.25.

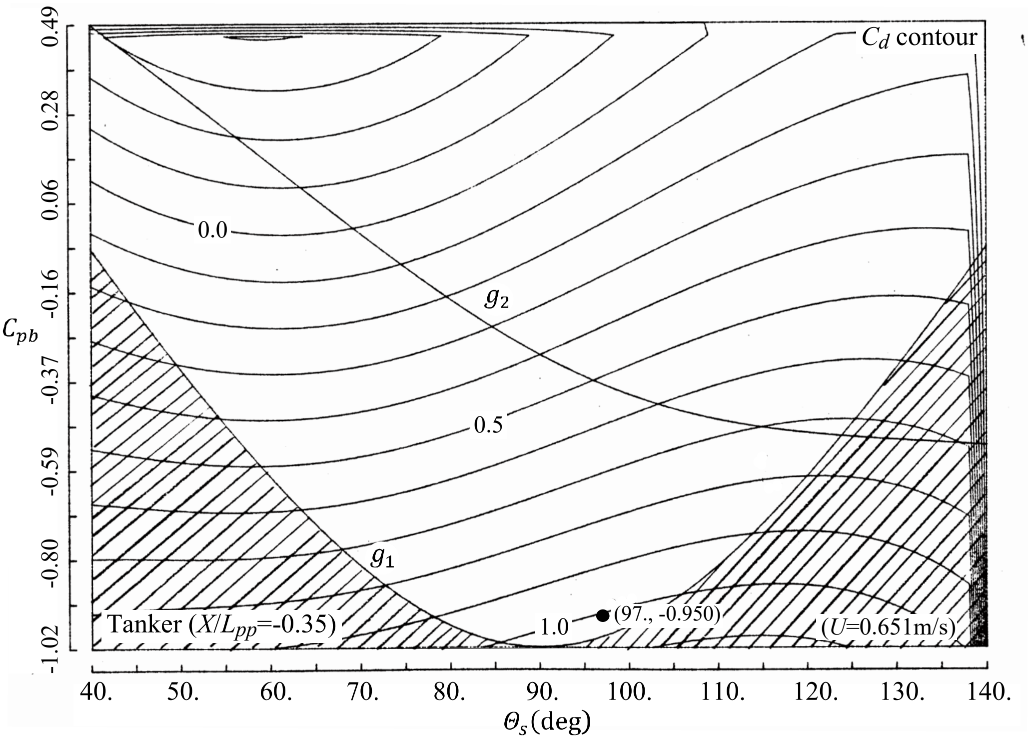

Fig. 4.3.15 Tanker's C_d (Θ_s, C_{pb}) at X/L_{pp}=-0.35.

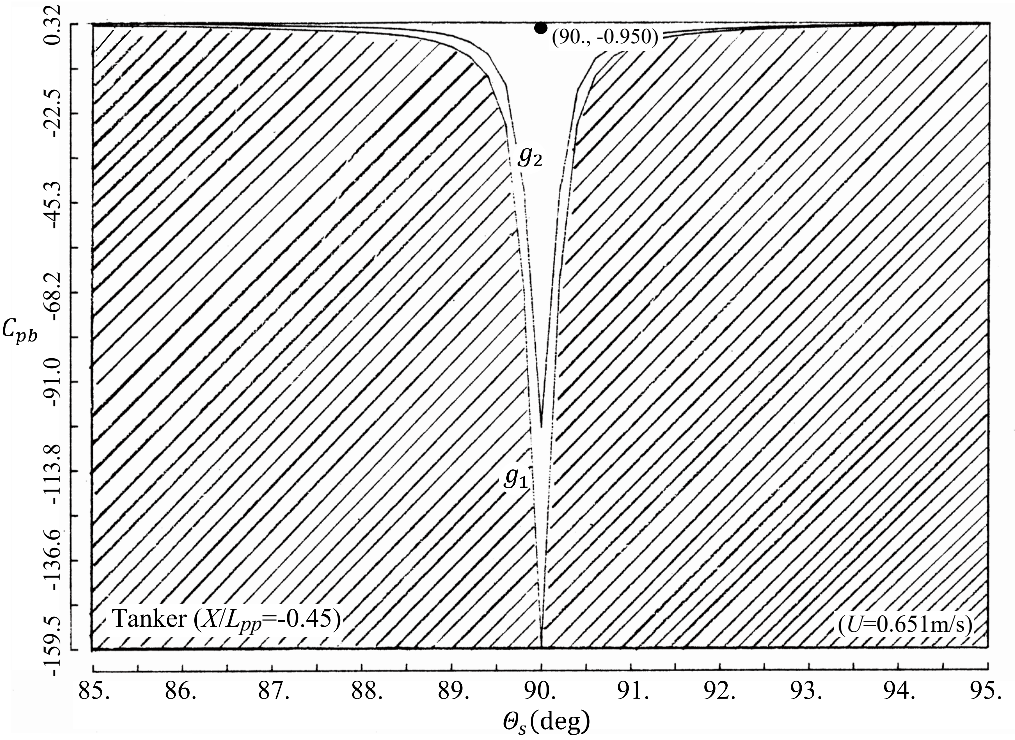

Fig. 4.3.16 Tanker's C_d (Θ_s, C_{pb}) at X/L_{pp}=-0.45.

4.4 C_d comparison with tank test data

Two-dimensional drag coefficients along ship length are shown in Figs. 4.4.1 and 4.4.2 compared with the tank test data for the containership and the tanker, respectively. Although no calculation result is obtained at the aft-end cross-section, the enhanced wake source model explains well the characteristics of the containership's tank test data. For the tanker, the enhanced wake source model also explains the tank test data except for the fore-end and the aft-end cross-sections. The discrepancy at the fore-end cross-section is probably due to the three-dimensional effect. The discrepancy at the aft-end cross-section is due to both the three-dimensional effect and poor Lewis form approximation, especially around the center keel.

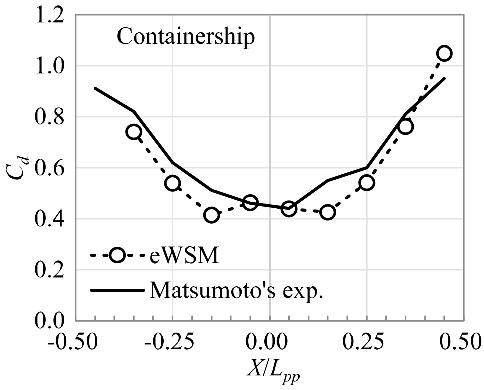

Fig. 4.4.1 C_d distribution of containership.

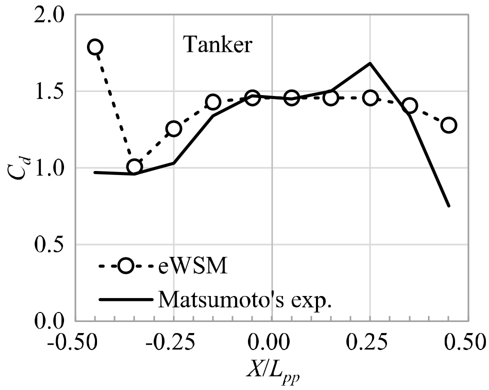

Fig. 4.4.2 C_d distribution of tanker.

5. Concluding remarks

This paper presented the analytical procedure to apply Parkinson's wake source model[13] to potential flow around ship cross-sections. Lewis form[14] approximated the ship cross-sections. The analysis clarified difficulties in the application that mainly occur in flow that separates around the upstream bilge corner of thick cross-sections or center keel of thin cross-sections. The present study proposed the enhanced wake source model and resolves the difficulties. Applications of the enhanced wake source model to the containership and the tanker using assumed base pressure and separation points show the appropriate separated streamlines and pressure distributions for cross-sections with adequate Lewis form approximations. The study discusses the effect of the separation point and the base pressure in the downstream region on the drag coefficient of the ship cross-sections. Comparison of the sectional drag coefficient distributions along ship length with tank test data of the segmented ship models[11,12] validated and showed the potential of the extended wake source model.

Acknowledgements

The author is grateful to the late Professor Emeritus HAMAMOTO Masami of Osaka University for his past advice on the publication of this study. The author is also grateful to Dr. MATSUMOTO Norihiro for his permission to use the ship hull form data of the subject ships and publish the calculation results.

References

1) Fedyaevsky, K. K. & Sobolev, G. V., Application of the solution of some steering problems, Symposium on the behaviour of ships in a seaway at Wageningen (1957).
2) Yoshimura, Y., Nakao, I., and Ishibashi, A., Unified mathematical model for ocean and harbour manoeuvring, Proc. of MARSIM (2009).
3) Sawada, R., et al., Path following algorithm application to automatic berthing control, J. of Marine Science and Technology 26-2 (2021) pp. 541-554.
4) Miyauchi, Y., et al., System parameter exploration of ship maneuvering model for automatic docking/berthing using CMA-ES, J. of Marine Science and Technology 27 (2022) pp. 1065-1083.
5) Oltmann, P. & Sharma, S, Simulation of combined engine and rudder manoeuvres using an improved model of hull-propeller-rudder interactions, 15th Symposium on Naval Hydrodynamics (1984).
6) Umeda, N. & Yamakoshi, Y., Hydrodynamic forces acting on a longitudinally non-symmetric ship under manoeuvring at low speed, J. of the Kansai Society of Naval Architects of Japan 211 (1989) pp. 127-137.
7) Tanaka, S., On hydrodynamic forces acting on a ship at larger drift angles, Transactions of the West-Japan Society of Naval Architects, 91 (1995) pp. 81-94.
8) Kijima, K. & Tanaka, S., Numerical study of cross flow drag by vortex shedding model, J. of the Japan Society of Naval Architects 170 (1991) pp. 235-243.
9) Kijima, K. & Tanaka, S., The cross flow drag acting on rectangular cross-sections with round edge, J. of the Japan Society of Naval Architects 172 (1992) pp. 1-8.
10) Tanaka, S. & Kijima, K., On the distribution of cross flow drag over the length of a ship moving transversely, J. of the Japan Society of Naval Architects, (1993) 174 pp. 357-363.
11) Matsumoto, N. & Suemitsu, K., Hydrodynamic force acting on a hull in maneuvering motion, J. of the Kansai Society of Naval Architects of Japan 190 (1983) pp. 35-44.

12) Matsumoto, N., Mathematical model of manoeuvring hydrodynamic forces and estimation of manoeuvrability of ships, Doctoral dissertation (1983) Osaka Univ.

13) Parkinson, G. V. & Jandali, T., A wake source model for bluff body potential flow, J. of Fluid Mech. 40-3 (1970) pp. 577-594.

14) Lewis, F. M., The inertia of the water surrounding a vibrating ship, Transactions of the SNAME 37 (1929) pp. 1-20.

15) Ueno, M., Research on hydrodynamic forces acting on ships in slow manoeuvring motion, Master's thesis (1984) Osaka Univ.

16) Woods, L. C., The theory of subsonic plane flow, Cambridge University Press (1961).